## RESEARCH ARTICLE

**Key Points:**
- Flexural slip occurs predominantly in well-layered, although uncommonly can develop in poorly layered beds
- Bed dips of ~30–100° and slip-surface spacings of ~10–440 m facilitate accumulation of flexural slip
- Irrespective of hinge migration, limb rotation is generally required to produce significant flexural-slip fault scarps

# Active Flexural-Slip Faulting: Controls Exerted by Stratigraphy, Geometry, and Fold Kinematics

Tao Li[1,2] (ID), Jie Chen[2] (ID), Jessica A. Thompson Jobe[3,4] (ID), and Douglas W. Burbank[3] (ID)

[1]Guangdong Provincal Key Lab of Geodynamics and Geohazards, School of Earth Sciences and Engineering, Sun Yat-Sen University, Guangzhou, China, [2]State Key Laboratory of Earthquake Dynamics, Institute of Geology, China Earthquake Administration, Beijing, China, [3]Department of Earth Science, University of California, Santa Barbara, CA, USA, [4]Institute of Tectonic Studies, Department of Geological Sciences, University of Texas at El Paso, El Paso, TX, USA

**Abstract** Flexural slip plays an important role in accommodating fold growth, and its topographic expression, flexural-slip fault (FSF) scarps, may be one of the most commonly occurring secondary structures in areas dominated by active thrusts and folds. Where FSF scarps are present and what factors control their occurrence, however, are typically poorly known. Through an investigation of clearly expressed FSF scarps, well-preserved fluvial terraces, and well-exposed bedrock at eight sites in the Pamir-Tian Shan convergent zone and Kuche fold belt, NW China, we summarize the most favorable conditions for active flexural-slip faulting. Our study yields six key results. First, flexural slip operates commonly in well-layered beds, although uncommonly can occur in massive, poorly layered beds as well. Second, in well-layered beds, the slip surface is commonly located either (a) close to the contact of competent and incompetent beds or (b) within thin incompetent beds. Third, FSF scarps are always found overlying steep beds with dips of ~30–100°. Fourth, slip surfaces are typically spaced between ~10 and 440 m but can reach up to ~600 m. Fifth, FSF scarps at most sites can be observed far away from the hinge-migrated fold scarps, suggesting that compared to hinge migration, limb rotation is generally required to accumulate flexural slip and produce associated topographic scarps. Finally, a higher regional convergent rate seems to facilitate the creation of FSF scarps more often than lower rates, whereas well-preserved, old terraces capped by thin deposits are more likely to record FSF scarps than unevenly preserved, young terraces with thick sedimentary caps.

## 1. Introduction

Folding deformation in fold-and-thrust belts commonly involves multiple operative mechanisms. As a result of limb rotation and/or hinge migration during shortening and uplift (e.g., Brandes and Tanner, 2014; Poblet, 2012; Shaw et al., 2005), locally accommodated stresses (e.g., via bed-parallel shear and bending-moment extension or contraction (also called orthogonal flexure that can produce tangential longitudinal strain)) can produce a number of secondary structures (e.g., Philip and Meghraoui, 1983; Tavani et al., 2015). Due to feedback, these secondary structures will influence fold development, for example, the fold geometry, the causative fault plane formation, and upward propagation (Mitra, 2002; Niño et al., 1998; Roering et al., 1997). Diverse mechanisms work together to produce various folding-related geomorphic expressions, such as fold scarps (e.g., Hubert-Ferrari et al., 2007; Le Béon et al., 2014; Li et al., 2015a; Thompson et al., 2002), land-surface tilting and warping (e.g., Daëron et al., 2007; Li et al., 2013; Rockwell et al., 1988; Saint-Carlier et al.,2016; Simoes et al., 2007), and flexural-slip and bending-moment fault scarps (e.g., Huang et al., 2015; Li et al., 2015b, 2016; Rockwell et al., 1984; Yeats et al., 1997), as well as an assemblage of different patterns (e.g., Ishiyama et al., 2004; Kelsey et al., 2008; Li et al., 2015b; Philip and Meghraoui, 1983).

Among all secondary structures, the flexural-slip fault (FSF), generated by bed-parallel slip in a well-layered sedimentary sequence, probably occurs most commonly (Figure 1). Such faults can develop in folds that deform by both limb rotation and hinge migration, during which the bed tends to retain constant thickness (Shaw et al., 2005; Tavani et al., 2015). In limb rotation (Figure 1a), flexural slip is initiated and accumulated as the limb continuously rotates to increase the bed curvature and tighten the fold. In hinge migration (Figure 1b), moving and bending of the bed within the hinge zone cause flexural slip until the bed enters an adjacent constant dip panel. Flexural slip can be active across the entire width of a deformed section and throughout almost its entire folding history (Behzadi & Dubey, 1980; Sanz et al., 2008) but dominantly operates where bed dips range from ~30 to 70° (Behzadi & Dubey, 1980; Gutiérrez-Alonson & Gross, 1999;
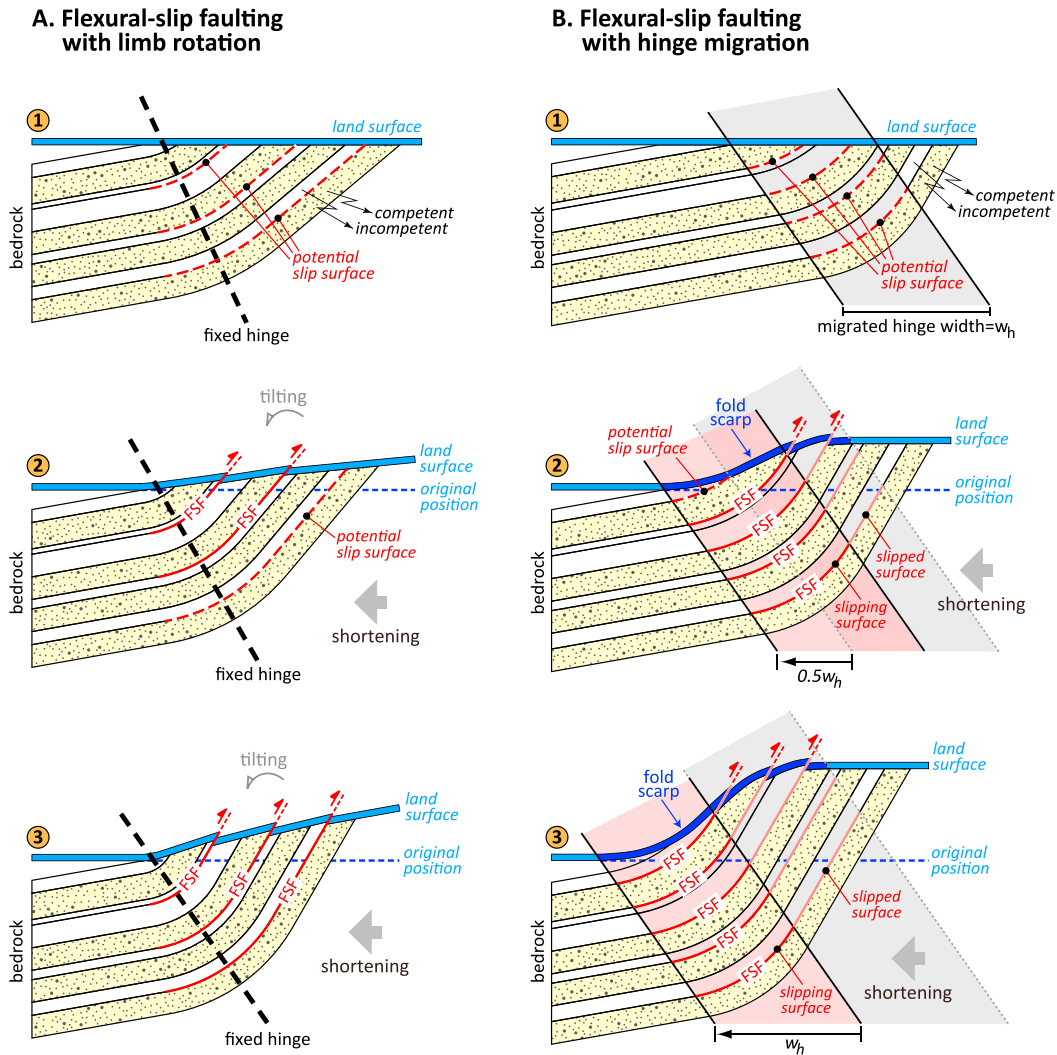
**Figure 1.** Schematic forward models of active flexural-slip faulting in conjunction with (a) limb rotation and (b) hinge migration. (a1 and b1) Initially, a planar land surface overlies a synclinal hinge, across which the bed dips in the same direction. (a2 and b2) During limb rotation, the limb and fixed hinge rotate to steepen the beds, tighten the fold, and tilt the overlying land surface. Migration of the hinge transports the bed through the hinge and differentially lifts the land surface to produce a fold scarp. Due to the imposed requirement of constant bed thickness, potential slip surfaces, commonly located along the contact between competent and incompetent beds, will be activated to cut through the land surface and produce topographic scarps. In limb rotation, the flexural-slip faults (FSFs) are distributed across the entire rotating limb. In hinge migration, flexural slip develops within the curved hinge zone as a result of bending of the bed. (a3 and b3) Continued limb rotation and hinge migration will result in (i) gradually tilting of the land surface and growth of the fold scarp, respectively, and (ii) breakthrough of new slip surfaces. Flexural slip and associated topographic scarp heights increase with progressive limb rotation. Conversely, the flexural slip and FSF scarp growth can continue when the bed migrates within the hinge zone, but will cease immediately after the bed enters the adjacent steep dip panel. From then on, the former slip surfaces (light red lines) preserved in the beds and FSF scarps on the land surface will be passively transported and lifted. These models demonstrate the permissible kinematic association of surface observations of FSF scarps, land-surface tilting, and hinge-migrated fold scarp. Modified after Shaw et al. (2005) and Tavani et al. (2015).

Ramsay, 1974): flexural slip is too weak before the bed attains a dip of ~30° and will almost terminate because of high frictional resistance between beds when the dip exceeds a critical value of ~60–70°.

In areas dominated by active folds, the FSFs can displace the land surface to produce an array of subparallel, potentially closely spaced topographic scarps, which are visually distinctive and are easily detected in field observations and satellite images (e.g., Yeats et al., 1997; Li et al., 2015b). In contrast to FSFs in bedrock that record the cumulative amount of flexural slip, FSF scarps on a geomorphic surface record a snapshot and an

**Table 1**

*A Summary of Locations of FSF Scarps Reported in the Current and Previous Studies, as Well as Their Underlying Bed Dip, Slip-Surface Spacing, and Associated Folding Mechanism*

| Location | Bed dip[a] | Slip-surface spacing[b] | Folding mechanism | References cited |
|---|---|---|---|---|
| Santa Clara syncline, California | 63–130° | 57–630 m | - | Yeats et al. (1981) |
| El Asnam Earthquake, Algeria | 80–90° | 33–66 m | - | Philip and Meghraoui (1983) |
| Ayers Creek syncline, California | ~42° | 170–418 m | limb rotation | Rockwell et al. (1984) |
| Ebro basin, Spain | ~40° | - | - | Casas et al. (1994) |
| Katakai, Niigata Prefecture, Japan | 56–74° | 10–37 m | - | Yeats et al. (1997) |
| Giles Creek, New Zealand | 70–85° | 67–235 m | - | Yeats et al. (1997) |
| Cape Arago region, central Oregon | 52–90° | 240–540 m | limb rotation | McInelly and Kelsey (1990) |
| Sardar fold, Tabas, eastern Iran | ~60° | - | - | Walker, Jackson, and Baker (2003) |
| Sierra de Villicum, San Juan, Argentina | ~40° | - | hinge migration | Krugh and Meigs (2003) |
| Kuwana anticline, central Japan | ~37° | 103–170 m | hinge migration | Ishiyama et al. (2004) |
| Seattle fault zone | 43–90° | 46–493 m | hinge migration | Kelsey et al. (2008) |
| Grand Hogback monocline, Colorado | 43–53° | 33–437 m | - | Gutiérrez et al. (2014) |
| Caijinchang, Mingyaole anticline | 45–60° | 12–20 m | hinge migration | this study |
| Kalangoulvke South, Mingyaole anticline | 50–66° | 10–137 m | hinge migration | this study |
| Kalangoulvke North, Mingyaole anticline | 65–82° | 10–149 m | hinge migration | this study |
| Kelatuo anticline | 76–82° | 9–84 m | - | this study |
| Wuheshalu syncline | 52–60° | 12–179 m | combined | this study |
| Northern limb of the Wulagen syncline | 48–86° | 55–142 m | limb rotation | this study |
| Biertuokuoyi monocline | 54–70° | 11–91 m | hinge migration | this study |
| Bashjiqike anticline, western China | 31–38° | 37–145 m | combined | this study |

[a]Bed dips larger than 90° because of the bed overturning.     [b]Slip-surface spacing calculated by map-view spacing of FSF scarps multiplied by sinusoidal value of the average bed dip.

incremental slip (typically occurring during several to perhaps hundreds of thousands of years) during the evolving history of a fold whose complete deformation history might itself span millions of years. As a result of different folding mechanisms, FSF scarps accordingly exhibit distinct characteristics (Figure 1): FSF scarps can be distributed across an entire fold limb during its rotation but tend to be restricted to the slope of the fold scarp during hinge migration (notably, this view contradicts our previous model (Li et al., 2015b) and, consequently, invalidates some conclusions associated with that model). Although flexural slip can commonly be detected in bed outcrops (e.g., Gutiérrez-Alonson & Gross, 1999; Horne & Culshaw, 2001; Tanner, 1989), the presence of FSF scarps appears to be much more limited: to date, only a few sites of FSF scarps have been identified and reported (listed in Table 1). Where FSF scarps commonly occur and what conditions facilitate their occurrence are typically poorly known.

Along the Pamir and southern Tian Shan piedmonts, NW China, where active thrusting and folding are widespread, numerous sets of strikingly clear FSF scarps are present on fluvial terrace surfaces (Figure 2). The underlying bedrock is well exposed, making it straightforward to constrain its geometry and lithology. This clarity provides an excellent opportunity to investigate the conditions that favor active flexural-slip faulting. Based on interpretation of Google Earth© images, detailed geologic and geomorphic mapping, along with differential GPS topographic measurements, we surveyed FSF scarps and associated terrace treads, as well as bedrock lithology and fold geometry at five new sites (Kalangoulvke North, Kelatuo, Wuheshalu and Biertuokuoyi South in the Pamir-Tian Shan convergent zone, and Bashjiqike in the Kuche fold belt; Figure 2). In order to expand the database of FSF scarps, observations of bedrock lithology and its association with flexural slip surfaces have also been added to three sites (Caijinchang, Kalangoulvke South, and Wulagen in the Pamir-Tian Shan convergent zone; Figure 2b) where the topographic expression of FSF scarps was reported in Li et al. (2015b). Integrating these results with existing data, we attempt to summarize the most favorable conditions that promote the presence of FSF scarps.

## 2. Tectonic Setting

The Tarim basin is one of the largest intracontinental basins in central Asia (Figure 2a). As a result of the Indo-Eurasian collision, the Pamir and southern Tian Shan that delineate the southwestern and northern margins of the basin, respectively, began to uplift since the late Oligocene-early Miocene (Burtman & Molnar, 1993;
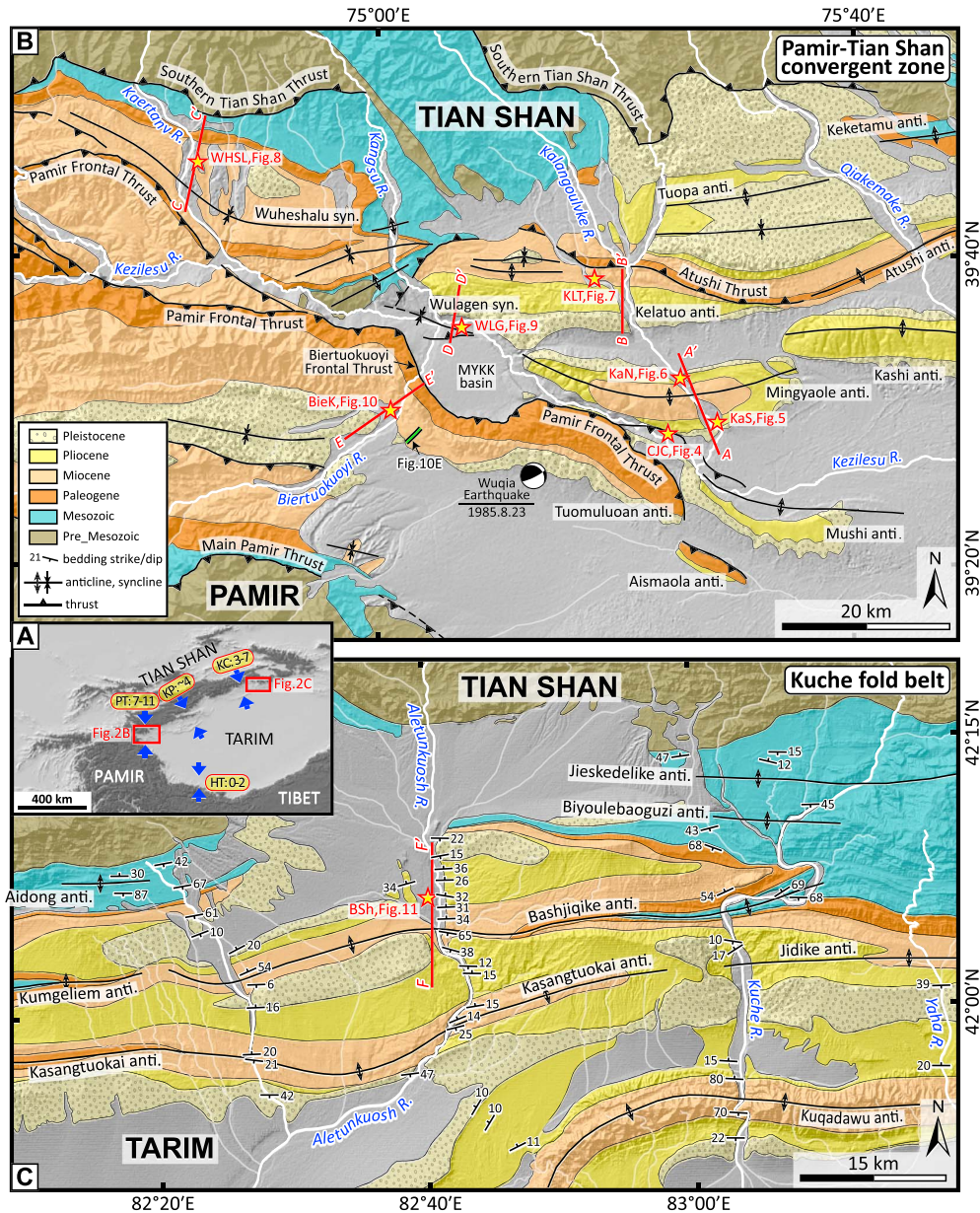
**Figure 2.** (a) Topographic map of central Asia. The yellow elliptical boxes show the modern convergent rates in the Hetian (HT), Kuche (KC), and Kepintagh (KP) fold belts and the Pamir-Tian Shan convergent zone (PT) determined from geological and geodetic GPS data (Hubert-Ferrari et al., 2007; Li et al., 2012, 2015a, 2016; Saint-Carlier et al., 2016; Yang et al., 2008; Zubovich et al., 2010). (b and c) Geologic maps of the Pamir-Tian Shan convergent zone and the Kuche fold belt, NW China. The focal mechanism solution of the 1985 Wuqia event from USGS seismic catalog. See Figure 2a for map locations. Major study sites are shown by yellow stars, and structure sections are indicated by red lines. BieK: Biertuokuoyi, Bsh: Bashjiqike, CJC: Caijinchang, KaN: Kalangoulvke North, KaS: Kalangoulvke South, KLT: Kelatuo, MYKK: Mayikake, WHSL: Wuheshalu, WLG: Wulagen.

Sobel et al., 2013; Sobel et al., 2006; Yin et al., 1998) and subsequently propagated forelandward to produce a suite of fold-and-thrust belts (Allen et al. 1999; Heermance et al., 2008; Thompson et al., 2015; Wang et al., 2011; Wang & Wang, 2016). Synchronous with this tectonic process, the Tarim basin has experienced striking subsidence as it was infilled by an up to 8 km thick, coarsening upward sedimentary sequence (Jia et al., 2004); has transitioned gradually from marine to continental deposition (Bosboom et al., 2014; Sun

et al., 2016; Wei et al., 2013); and has rotated clockwise due to compression along its irregular boundaries (Avouac et al., 1993; Zubovich et al., 2010).

At the westernmost of the Tarim basin (Figure 2b), the Pamir Frontal Thrust and the Atushi-Kashi fold belt, which are respectively formed along the deformation leading edge of the Pamir and southern Tian Shan, interfere with each other approximately along the course of the Kezilesu River, the largest longitudinal river in the region. This interference zone is characterized by pronounced Quaternary thrusting and folding. Geomorphic surfaces in the zone are significantly deformed by mechanisms of emergent thrusting, hinge migration, limb rotation, and flexural-slip faulting (Heermance et al., 2008; Li et al., 2012; Li et al., 2013, 2015a, 2015b; Scharer et al., 2006). A geologically and geodetically determined convergent rate of ~7–11 mm/a (Li et al., 2012, 2015a; Yang et al., 2008; Zubovich et al., 2010) and the 1985 Wuqia $M_w$7.0 event triggered by the Pamir Frontal Thrust (Feng, 1994) reflect this narrow zone's ongoing and concentrated activity.

Approximately 700 km to the east of the Pamir-Tian Shan convergent zone, the Kuche fold belt along the southern Tian Shan piedmont includes a succession of well-exposed folds (Figure 2c). Quaternary deformation in this fold belt is also dominated by mechanisms of hinge migration and limb rotation (e.g., Hubert-Ferrari et al., 2007; Saint-Carlier et al., 2016; Wang et al., 2011), but significant emergent thrusting is largely absent. The convergent rate is loosely determined to be ~3–7 mm/a from geological and geodetic data (Hubert-Ferrari et al., 2007; Saint-Carlier et al., 2016; Yang et al., 2008): significantly slower than that in the Pamir-Tian Shan convergent zone.

## 3. Field Data Collection and Kinematic Model of Terrace Deformation

### 3.1. Field Techniques and Data Collection

A flexural-slip fault requires that its slip surface is localized along the bed plane. In this study, except at Kalangoulvke South and North at Mingyaole where fault outcrops explicitly reveal such slip, fault scarps at other sites are classified as flexural slips according to their typical, as well as site-specific, flexural-slip characteristics (Yeats et al., 1997): (i) the scarps are numerous and closely spaced, (ii) they strike parallel with underlying beds and commonly display straight and linear trends, and (iii) upper beds slip over underlying beds toward anticlinal hinges and away from synclinal hinges, such that each fault's hanging wall lies on the side of the synclinal hinge.

To investigate the potential controlling factors of active flexural-slip faulting, several data sets have been collected: (i) the overall fold geometry, (ii) fluvial terrace distribution and classification, (iii) topography of terrace treads and fault scarps, (iv) geometry of folded beds underlying fluvial terraces, and (v) bed lithology associated with FSFs.

Lithified beds have been significantly uplifted and well exposed in the study area (Figure 2). We carried out structural mapping along major water gaps which provided easy access to fold transects. The fold geometry was simplified using kink-style hinges to separate dip panels, except at the Wulagen fold where a wide, curved hinge zone was loosely defined due to the rarity of bed outcrops. Panel width and inclination were determined by grouping dip data into internally consistent sets and calculating their average angle. The hinge was assigned to bisect the interpanel angle.

Vertical downcutting and lateral planation of the Kezilesu River, its major tributaries (e.g., Kaertanv, Kangsu, Biertuokuoyi, and Kalangoulvke Rivers), and the Aletunkuosh River have created flights of fluvial terraces (Figure 2). These terraces overlie strongly deformed beds and are presently capped by up to tens-of-meter-thick gravels with uncommon sand lenses. Based on interpretations of Google Earth© images and additional field calibration, we classified fluvial terraces into several main divisions referring to (i) relative height with respect to each other and the modern riverbed, (ii) surface morphology (older surfaces characterized by better developed desert pavement, higher degree of weathering, and more tightly packed clasts), and (iii) existing chronologic results (Li et al., 2012, 2015a; Thompson, 2013). Certain terraces can be further divided into several sublevels as distinguished by minor height variations. No attempt was made to correlate fluvial terraces among different river valleys.

Fluvial terraces can serve as excellent geomorphic markers to record recent faulting and folding deformation. We measured the topography of terrace treads using a differential GPS system with relative vertical and
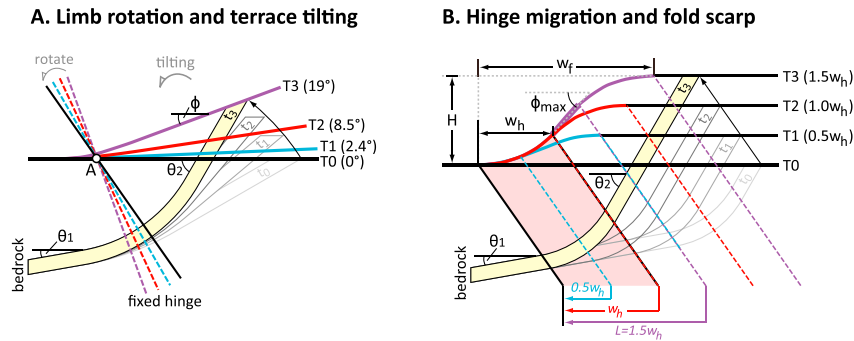
**Figure 3.** Terrace deformation patterns due to (a) limb rotation and (b) hinge migration. The gray outlined and yellow beds are, respectively, prior to and after folding deformation. Terraces T3, T2, and T1 correlate with the bed rotating or migrating from positions $t_0$ to $t_3$, $t_1$ to $t_3$, and $t_2$ to $t_3$, respectively, and terrace T0 indicates the modern riverbed. Rotation of the bed and hinge tilts overlying fluvial terraces (Figure 3a). Rotation of the hinge can migrate some beds from the steep-dipping panel to the right of the hinge into the gently dipping panel to the left of the hinge (Poblet et al., 1997; Poblet & McClay, 1996; Scharer et al., 2006), so that the terrace tilt is lower than the limb rotation (see Appendix A). We require the hinge to rotate around the point "A" on the land surface because, if not, rotation of the hinge can produce a tiny topographic scarp theoretically (Figure 4 in Scharer et al., 2006), which still has not been convincingly observed from natural cases. To simplify the model and avoid some unnecessary confusion between this type of topographic scarps and hinge-migrated fold scarps, we fix the rotation center on the land surface. Progressive rotation causes successively emplaced terraces (T3 to T0) to fan across the limb. Migration of the hinge transports the bed through the hinge and differentially lifts the land surface to produce a fold scarp (colored lines) (Figure 3b). Along with increases in height ($H$) and width ($w_f$), the fold scarp steepens gradually until the hinge migration distance ($L$) exceeds the hinge width ($w_h$). As a result, the height and width of the fold scarp tend to increase from T0 to T3, whereas the fold-scarp slope on T2 is larger than that on T1, but similar to that on T3. Away from the fold scarp, fluvial terraces lie parallel with each other. $\phi_{max}$: the scarp-slope maximum.

horizontal precisions of <4 cm: less than the geomorphic noise due to natural ground irregularities. We strove to walk survey paths approximately straight, continuous, and oriented perpendicular to the fold axis or fault trace. Areas mantled by young colluvium, areas of artificial modifications, and outer terrace edges where the tread was apparently eroded were avoided.

The fine-scale bed geometry beneath fluvial terraces was determined through closely spaced dip measurements. Because terrace deformation is closely related to hinge width (e.g., Chen et al., 2007; Hubert-Ferrari et al., 2007; Li et al., 2015a; Suppe et al., 1997), we identified (where appropriate) a curved hinge zone, rather than a kink-style hinge, to help characterize the overall fold geometry. The measured bed geometry was integrated with the topographic survey profiles, such that the deformation pattern of fluvial terraces can be directly associated with underlying structures. At Mingyaole South, Kelatuo, and Biertuokuoyi, the bedrock is clearly and continuously exposed along terrace risers or deeply incised valleys. We logged simplified sedimentary sequences both to distinguish among mudstone, sandstone, and conglomerate and to identify flexural-slip surfaces that produce related topographic scarps: the latter enables a confident correlation between flexural-slip surfaces and specific bed lithologies.

### 3.2. Terrace Deformation in Mechanisms of Limb Rotation and Hinge Migration

Although locally disturbed by flexural-slip faulting (Figure 1), passively deformed fluvial terraces that span a fold can serve to differentiate the mechanisms of limb rotation and hinge migration (e.g., Daëron et al., 2007; Lavé & Avouac, 2000; Li et al., 2013; Li et al., 2015a; Saint-Carlier et al., 2016; Scharer et al., 2006; Simoes et al., 2007; Thompson et al., 2002). During limb rotation (Figure 3a), fluvial terraces are tilted in the same direction as underlying beds. In an individual dip panel, the tilt angle increases for the succession of young to old terraces (Scharer et al., 2006). Because some beds can migrate through the hinge as a result of its rotation (Poblet et al., 1997; Poblet & McClay, 1996; Scharer et al., 2006), the terrace tilt ($\phi$) is commonly lower than the bed rotation ($\phi'$) (see Figure 3a and Appendix A). Both parameters have a geometric relationship (see Appendix A):

$$\tan\left(\frac{\theta_2+\theta_1}{2}-\phi\right) = \frac{\sin\left(\theta_2-\phi'\right)\cos\left(\frac{\theta_2-\theta_1-\phi'}{2}\right)}{\cos\left(\frac{\theta_2-\theta_1}{2}\right)\left[\cos\left(\frac{\theta_2+\theta_1-\phi'}{2}\right)\cos\left(\frac{\theta_2-\theta_1}{2}\right)-\sin\left(\theta_2-\phi'\right)\sin\left(\frac{\phi'}{2}\right)\right]} - \tan\left(\frac{\theta_2-\theta_1}{2}\right), \quad (1)$$

where $\theta_2$ and $\theta_1$ are the bed dips. Practically, the terrace tilt (difference between the present and initial slopes) cannot be directly determined from its outcrop angle, however, because the initial slope is

commonly unknown. In this study, we assume the modern riverbed gradient at each site to represent the initial slope of all fluvial terraces, and then to calculate the amount of subsequent terrace tilting and limb rotation (e.g., Scharer et al., 2006). Given that the river gradient may change as a result of subsequent water or sediment discharge variations or the rate changes of base level fall during the fold's evolving history (e.g., Lavé & Avouac, 2001; Malatesta et al., 2016; Poisson & Avouac, 2004), this assumption may introduce some uncertainty in the evaluation of limb rotation.

Migration of the hinge transports the bed through the hinge and differentially lifts the land surface to produce a topographic fold scarp (Figure 3b) (Chen et al., 2007; Hubert-Ferrari et al., 2007; Li et al., 2015a). At the beginning of growth, the scarp slope, height, and width increase gradually with hinge migration. The fold scarp width ($w_f$), fold scarp height ($H$), hinge migration distance ($L$), and hinge width ($w_h$) have a geometric relationship:

$$w_f = L + w_h - H^* \tan\left(\frac{\theta_2 + \theta_1}{2}\right) \tag{2}$$

When the hinge-migration distance exceeds the hinge width, the scarp slopes approach the maximum steepness ($\phi_{max}$; Figure 3b) dictated by underlying bed dips ($\theta_2$ and $\theta_1$):

$$\tan\left(\frac{\theta_2 + \theta_1}{2} - \phi_{max}\right) = \tan\left(\frac{\theta_2 + \theta_1}{2}\right) - 2\tan\left(\frac{\theta_2 - \theta_1}{2}\right) \tag{3}$$

Away from the fold scarp, fluvial terraces lie parallel with each other. If the bed is transported along the causative fault plane, the incremental fault slip ($S$) can be calculated from the fold scarp height ($H$) (Chen et al., 2007; Hubert-Ferrari et al., 2007):

$$S = H/(\sin\theta_2 - \sin\theta_1) \tag{4}$$

Overall, the increasing height and width of the fold scarps neighboring the hinge, the geometric relationship of the slope and underlying bed dips, and the parallelism of fluvial terraces away from the fold scarp can be diagnostic of the hinge migration from limb rotation (Figures 1 and 3). Using these criteria, we distinguish hinge-migrated fold scarp at our studied sites.

## 4. Active Flexural-Slip Faulting at Mingyaole

### 4.1. The Mingyaole Anticline

The Mingyaole anticline lies along the deformation front of the southern Tian Shan foreland thrust system (Figure 2b). On the surface, the fold is expressed topographically by its southward arcuate relief that extends eastward for ~36 km. The southwestern edge of the fold is impinged upon by the Tuomuluoan anticline along the Pamir Frontal Thrust. To the east, the Mingyaole South Thrust, a northern branch of the Pamir Frontal Thrust, ruptured Mingyaole's southern flank during the 1985 $M_w$7.0 Wuqia earthquake (Figures 2b and 4a) (Feng, 1994). The south flowing Kalangoulvke River, joining with the SE flowing Kezilesu River, orthogonally and obliquely bevels the fold, respectively, to create flights of fluvial terraces (Figures 4–6).

Along the Kalangoulvke water gap (transect A-A', see Figure 2b for the location), the Mingyaole fold is a geometrically simple, slightly north vergent fold with an ~70° dipping northern limb and an ~58° dipping southern limb (Figure 4a inset) (Chen et al., 2005; Li et al., 2015a). Lithified sedimentary sequences exposed in the fold include the following: tan, brownish interbedded mudstone and fine sandstone of the Miocene (N1); gray-yellow and gray-green coarse sandstone alternating with mudstone of the Pliocene (N2); and characteristic, dark gray, massive pebble-cobble conglomerate of the Pleistocene (Q1) (Figure 2b). The Mingyaole fold remains highly active. Fluvial terraces across the fold exhibit significant deformation by folding, for example, warping, fold scarps, and FSF scarps, at Caijinchang and Kalangoulvke water gap (Chen et al., 2005; Li et al., 2015a, 2015b; Scharer et al., 2006). An analysis of the fold-scarp geometry defines a Holocene shortening rate of ≥5.0 mm/a, implying that more than half of the regional convergent rate has been accommodated by this fold (Li et al., 2015a).
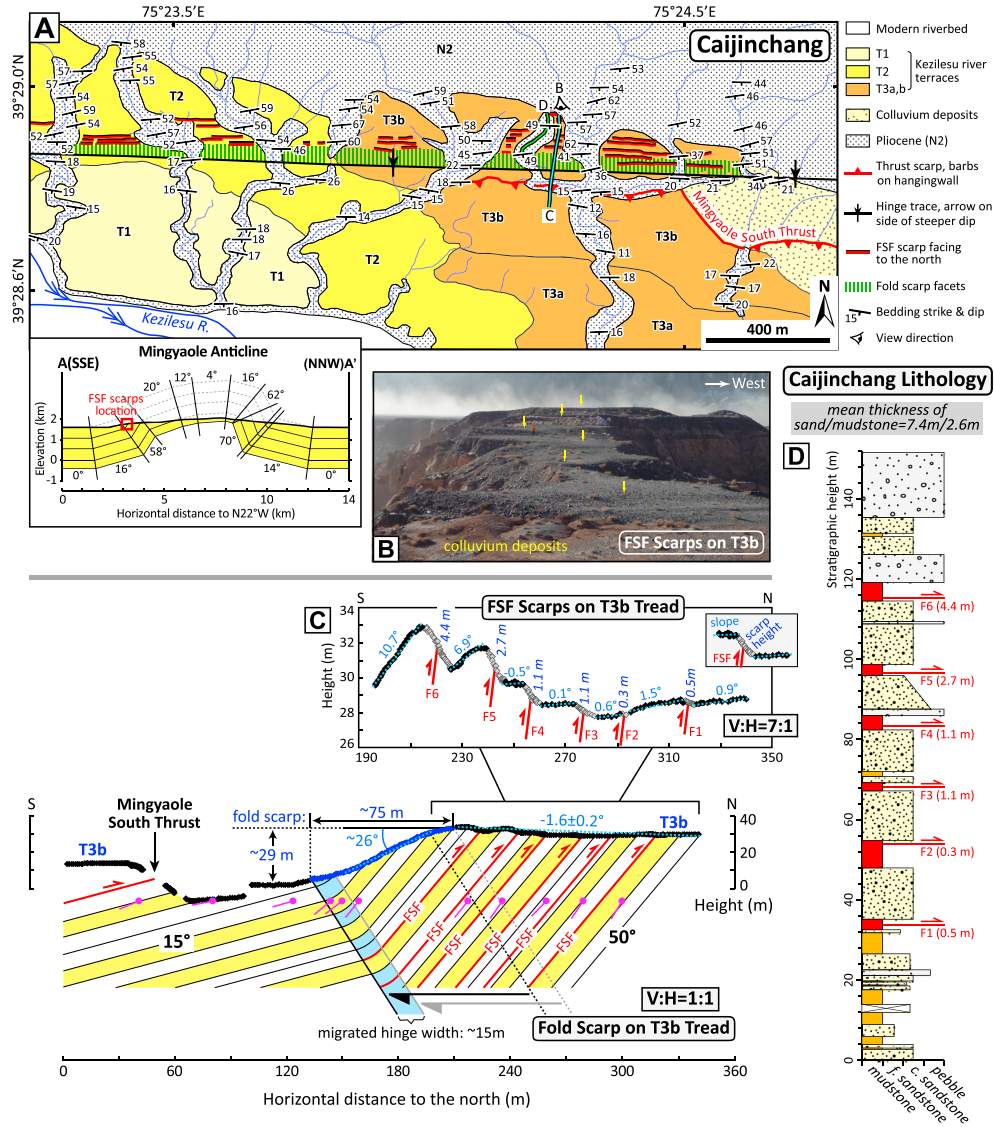
**Figure 4.** (a) Geologic and geomorphic map of the Kezilesu River terraces at Caijinchang on Mingyaole southern limb, as interpreted from Google Earth images and field data. Inset A-A' shows the cross section of the Mingyaole fold along the Kalangoulvke water gap. See Figure 2b for locations of the mapping area and cross section. (b) Photograph (viewpoint in Figure 4a) of FSF scarps (yellow arrows) on the T3b tread. (c) Topographic survey profile of the fold scarp and FSF scarps on the T3b tread and associated folded bed geometry. Lower panel: bed dip, FSF dip, and fold-scarp slope with no vertical exaggeration; upper panel: terrace surface slopes and FSF dips are vertically exaggerated to show vertical displacements on individual faults. See Figure 4a for the profile location. (d) Correlation of flexural slip surfaces with bed lithology (fault numbers correlate with those in Figure 4c). The average thicknesses of sandstone and mudstone are ~7.4 and 2.6 m, respectively. All beds with slip surfaces are specified by a red color. See the logged section location (green line) in Figure 4a. Figures 4a and 4b are modified from Li et al. (2015b).

## 4.2. Caijinchang

Caijinchang is located on the southern limb of the Mingyaole fold and northern bank of the Kezilesu River (Figure 2b), where fluvial terraces encompass three major divisions (T3b/a, T2, and T1) (Figure 4a). Terrace treads are deeply dissected by south flowing ephemeral channels and are partially mantled by colluvium transported from adjacent bedrock relief to the north (Figure 4b). Dip measurements of bed outcrops define an ~15 m wide synclinal hinge that separates beds dipping 50–59°S in the north from those dipping 15–20°S in the south (Figure 4c). Migration of the hinge produces an ~29 m high, ~75 m wide, east trending fold scarp on the T3b tread (Figures 4a and 4c and Table 2) (Li et al., 2015a).
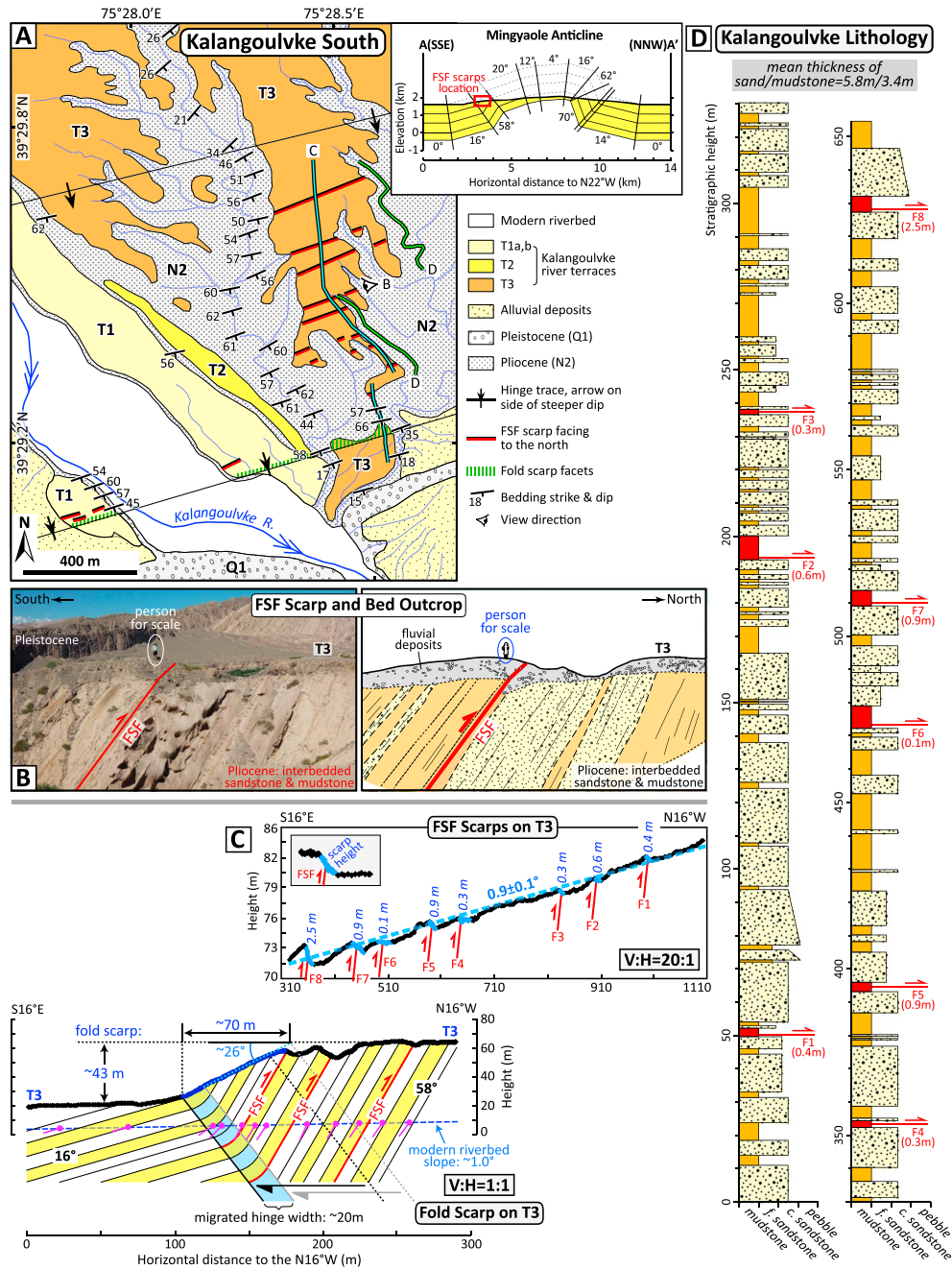
**Figure 5.** (a) Geologic and geomorphic map of the Kalangoulvke River terraces on Mingyaole southern limb. Inset shows the Mingyaole cross section. See Figure 2b for locations. (b) (left) Photograph and (right) sketch of a FSF outcrop on the T3 terrace riser (viewpoint in Figure 5a), illustrating that the Pliocene strata are characterized by interbedded sandstone and mudstone, and the flexural slip occurs near sand/mudstone contacts. (c) Topographic survey profile (location in Figure 5a) of a fold scarp and FSF scarps on the T3 tread and underlying folded bed geometry. The modern riverbed slope of ~1.0° from Scharer et al. (2006). (d) Correlation of flexural slip surfaces with bed lithology (the fault number is correlated with that in Figure 5c). The average thicknesses of the sandstone and mudstone are ~5.8 and 3.4 m, respectively. See Figure 5a for the section location (green lines). Figures 5a and 5c are modified from Li et al. (2015a, 2015b).

To the north of the synclinal hinge where underlying beds dip steeply (50–59°S), terrace surfaces are displaced by a group of north facing FSF scarps. These scarps are ~0.2–5.0 m high and are spaced from ~15 to 25 m apart (Figures 4a–4c). Although one to two scarps occur on the slope, all others occur on the
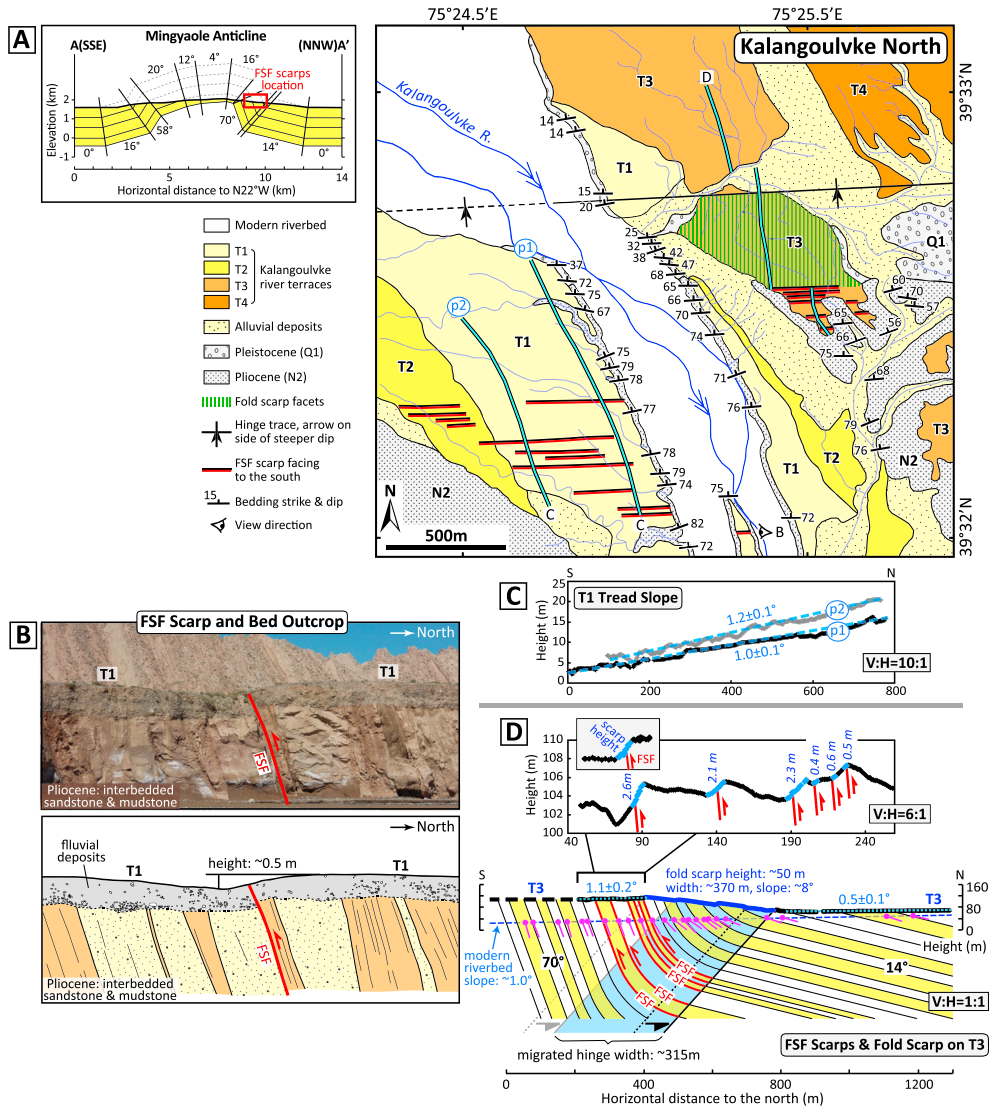
**Figure 6.** (a) Geologic and geomorphic map of Kalangoulvke River terraces on Mingyaole northern limb. Inset shows the Mingyaole cross section. Modified from Li et al. (2015a). See Figure 2b for locations. (b) Photograph (upper) and sketch (lower) of a FSF outcrop on the T1 terrace riser (viewpoint in Figure 6a), showing that the FSF slips along the sand/mudstone contact. (c and d) Topographic survey profiles of T3 and T1 treads correlated with folded bed geometry. The modern riverbed slope of ~1.0° from surveys by Scharer et al. (2006). See Figure 6a for profile location.

upper tread of the fold scarp. As described in Li et al. (2015b), the terrace tread appears to tilt southward overall, and the tilt angle generally decreases farther away from the hinge (Figure 4c). Given the limited spatial extent and strong disturbance of FSF scarps, the terrace treads cannot be used to evaluate the mechanism of limb rotation. However, accounting for the entire tread slope of 1.6 ± 0.2° to the north (Figure 4c), opposite to the dip direction of underlying beds, we speculate that the limb rotation is, if any, very minimal. This interpretation is further supported by observations at Kalangoulvke South (following section).

To explore the control of lithology on the presence of flexural slip surfaces, an ~150 m thick section of the Pliocene has been logged along a deep valley immediately to the west of the topographic profile (Figure 4d). The beds comprise relatively thick sandstone or sandy conglomerate alternating with thin mudstone, whose

**Table 2**
*A Summary of Parameters Associated With Terrace Tilting and Hinge-Migrated Fold Scarps Reported in This Study*

**Terrace tilting**

| Location | Dip panel | Riverbed gradient | Terrace slope | | Terrace tilt | Limb rotation |
|---|---|---|---|---|---|---|
| | | | Terrace | Slope | | |
| Caijinchang | 50°S | - | T3b | 1.6 ± 0.2°N | - | - |
| Kalangoulvke South | 58°S | Kalangoulvke: 1.0°S | T3 | 0.9 ± 0.1°S | 0.1°N | - |
| Kalangoulvke North | 70°N | Kalangoulvke: 1.0°S | T3 | 1.1 ± 0.2°S | 0.1°S | - |
| | | | T1 | 1.1 ± 0.1°S | 0.1°S | - |
| Kelatuo | 80°S | - | - | | - | - |
| Wuheshalu | 50°S | Kaertanv: 2.2 ± 0.1°S | T3b | 3.2 ± 0.1°S | 1.0°S | ~2.4° |
| | | | T1a | 2.3 ± 0.1°S | 0.1°S | ~0.3° |
| Wulagen North | 70°S | Kezilesu: 0° | T3a | 0.1–1.6°S | 0.1–1.6°S | >0.1–1.6° |
| | | Biertuokuoyi: 1.0 ± 0.1°N | T3b | 2.1 ± 0.1°S | 3.1°S | >3.1° |
| Biertuokuoyi | 62°SW | Biertuokuoyi: 1.4 ± 0.1°NE | T4 | 1.4 ± 0.1°NE | ~0° | ~0° |
| Bashjiqike | 34°N | Aletunkuosh: 0.5°S | - | | - | - |

**Hinge-migrated fold scarp**

| Location | Dip panel ($\theta_2/\theta_1$) | Fold scarp | | | | Hinge width | Predicted slope maximum[a] |
|---|---|---|---|---|---|---|---|
| | | Terrace | Height | Width | Slope | | |
| Caijinchang | 50°/15°S | T3b | 29 m | 75 m | 26°S | 15 m | 32° |
| Kalangoulvke South | 58°/16°S | T3 | 43 m | 70 m | 26°S | 20 m | 38° |
| Kalangoulvke North | 70°/14°N | T3 | 50 m | 370 m | 8°N | 315 m | 51° |
| Wuheshalu | 26°/10°S | T3a | 21 m | 350 m | 6°S | 280 m | 15° |
| Biertuokuoyi | 62°/50°SW | T4 | 70 m | 910 m | 5°SW | - | 4° |
| Bashjiqike | 34°/24°N | T4 | - | - | 6–8°N | - | 8° |
| | | T3a | 4.8 m | 190 m | 2°N | | |
| | | T2a | 1.3 m | 125 m | 1°N | | |

[a]Predicted slope maximum calculated from formula (3).

average thicknesses are ~7.4 and 2.6 m, respectively. Flexural slip surfaces either are located in mudstone layers as thin as 2.0–2.6 m (faults F1 and F3) (Figure 4d) or lie close to ($<$0.6 m) or along sand/mudstone contacts (faults F2, F4–6).

### 4.3. Kalangoulvke South

The synclinal hinge at Caijinchang can be traced eastward to the Kalangoulvke water gap (Figure 2b), where three terrace levels with different heights are present and are also deformed by a fold scarp and FSF scarps (Figure 5). The hinge in Pliocene and Pleistocene beds trends ENE and is ~20 m wide, bisecting the ~58°S dip panel in the north from the ~16°S dip panel in the south (Figure 5c).

The fold scarp neighboring the synclinal hinge has a slope of ~26°S, a height of ~43 m, and a width of ~70 m on the T3 tread (Figure 5c and Table 2). To the north of the fold scarp, at least nine FSF scarps occur in an ~800 m wide zone with spacings of ~12–160 m and heights of ~0.1–2.5 m (Figures 5a and 5c). Although locally disturbed by FSF scarps, the upper tread of T3 slopes 0.9 ± 0.1°S as a whole (Figure 5c), ~0.1° lower than the modern river gradient of ~1.0°S in Scharer et al. (2006), illustrating that the T3 tread appears to be slightly tilted opposite to the dip direction of underlying beds. This tilt disagrees with the predication of rotation of the ~58°S dip panel and demonstrates that the fold growth here is dominated by hinge migration. Because the ~50°S dip panel at Caijinchang is the western continuation of the ~58°S dip panel herein, it is reasonable to conclude that Caijinchang folding is also dominated by hinge migration, consistent with our previous interpretation.

As revealed by an ~650 m thick section (Figure 5d), the underlying Pliocene strata comprises thick sandstone with an average thickness of ~5.8 m interbedded with thin mudstone with an average thickness of ~3.4 m. The fault slides either (i) close to ($<$1.0 m) or along the sand/mudstone contacts (faults F1–F2 and F6–F8) (Figures 5b and 5d) or (ii) within thin mudstone layers with a thickness of ~1.6–2.8 m (faults F3–F5): behavior quite similar to observations at Caijinchang.

### 4.4. Kalangoulvke North

On the Mingyaole northern flank (Figure 2b), four terrace levels are preserved along the Kalangoulvke water gap (Figure 6a). On the T3 tread (Figures 6a and 6d), a north facing fold scarp is present with a height of ~50 m, a width of ~370 m, and a slope of ~8.0°N. This scarp is spatially associated with an ~315 m wide synclinal hinge in Pliocene and Pleistocene beds, across which the bed steepens southward gradually from ~14° to 70°N (Li et al., 2015a).

To the south of the hinge (Figures 6a and 6d), as many as six FSF scarps with heights of ~0.5–2.6 m displace the spatially limited T3 tread and more than 10 FSF scarps with heights of ~0.2–0.5 m displace the T1 tread. These faults are distributed across an ~1000 m wide zone with fault spacing of ~10 to 155 m. One fault exposure along the T1 riser shows that the fault slips along the sand/mudstone contact (Figure 6b). Although displaced by FSFs, the T3 tread slopes 1.1 ± 0.2°S overall: slightly steeper than both the T3 tread slope of 0.9 ± 0.1°S at Kalangoulvke South (Figure 5c) and the T1 tread slope of ~1.0–1.2°S herein (Figure 6c), as well as the modern fluvial slope of ~1.0°S (Scharer et al., 2006). Therefore, the tilt of the T3 tread also appears to be opposite of the bed dip direction, and the mechanism of hinge migration mainly accounts for the folding deformation.

## 5. Active Flexural-Slip Faulting at Kelatuo

### 5.1. The Kelatuo Anticline

Approximately 5 km to the north of the Mingyaole fold (Figure 2b), the Kelatuo anticline is orientated east for ~38 km from the Kangsu River to its surface termination plunging beneath the NE dipping Atushi Thrust. The Kalangoulvke River, draining south from the mountains of the southern Tian Shan, transversely crosses the east central portion of the fold.

Due to displacement along the Atushi Thrust, the Kelatuo northern limb is absent on the surface along the whole length of the fold, and the core crops out only at its western segment, which includes several highly deformed secondary folds (Figure 2b). By contrast, the southern limb is characterized by a well-exposed, prominent monocline (transect B-B′ in Figure 7a inset, see Figure 2b for the location): the bed dip decreases gradually from ~70–80° to 46°, 28°, and 0° down the length of the Kalangoulvke water gap. The fold reveals a sequence of lower Miocene through Pleistocene strata (Figure 2b), whose lithology is similar as that in the Mingyaole fold.

### 5.2. FSF Scarps and Terrace Deformation

Kalangoulvke terraces at Kelatuo can be separated into four major groups (Figure 7a). All terraces are preserved on the river's northern bank and overlie the ~80°S dip panel of the Miocene unit. On the terrace treads, more than 10 FSF scarps are present with spacing varying from ~10 to 86 m (Figure 7a) and heights of ~0.4 to 2.3 m (Figures 7b and 7c). As a consequence of ephemeral channel dissection and colluvial deposition (Figure 7a), the terrace tread slope is difficult to approximate to determine whether or not the ~80°S dip panel has rotated.

The strata underlying terrace treads at Kelatuo are much finer-grained than those at Mingyaole. Based on an ~490 m thick section of lower Miocene (Figure 7d), the lithology is characterized by thin sandstone with an average thickness of ~2.3 m and thick mudstone with an average thickness of ~6.3 m. In spite of the contrasting lithology, flexural slip surfaces are restricted to similar locations (Figure 7d): except for faults F3 and F5 that are located in mudstone layers as thick as ~12–55 m, all others are localized either close to (<1.0 m) sand/mudstone contacts (F1, F6–F8, and F11) or within thin mudstone layers of ~0.6–2.0 m thick (F2, F4, F9, and F10).

## 6. Active Flexural-Slip Faulting at Wuheshalu

### 6.1. The Wuheshalu Syncline

The Wuheshalu syncline lies between the southern Tian Shan Thrust to the north and the Pamir Frontal Thrust to the south (Figure 2b). Overall, the fold has a length exceeding 50 km and displays a gentle southward arcuate shape on the surface. Near the middle of this elongate fold, the south flowing Kaertanv River orthogonally crosses the fold to produce a wide water gap and multiple, nested fluvial terraces. Spatially coincident
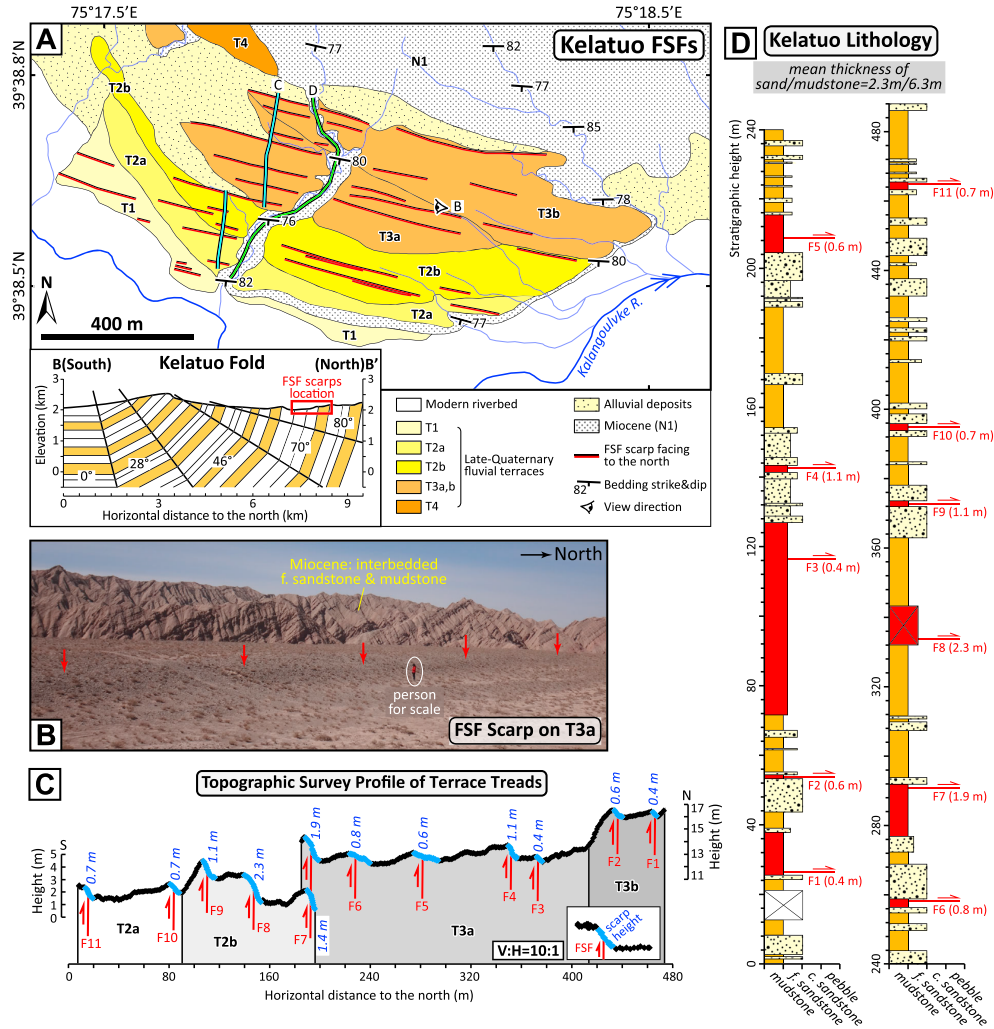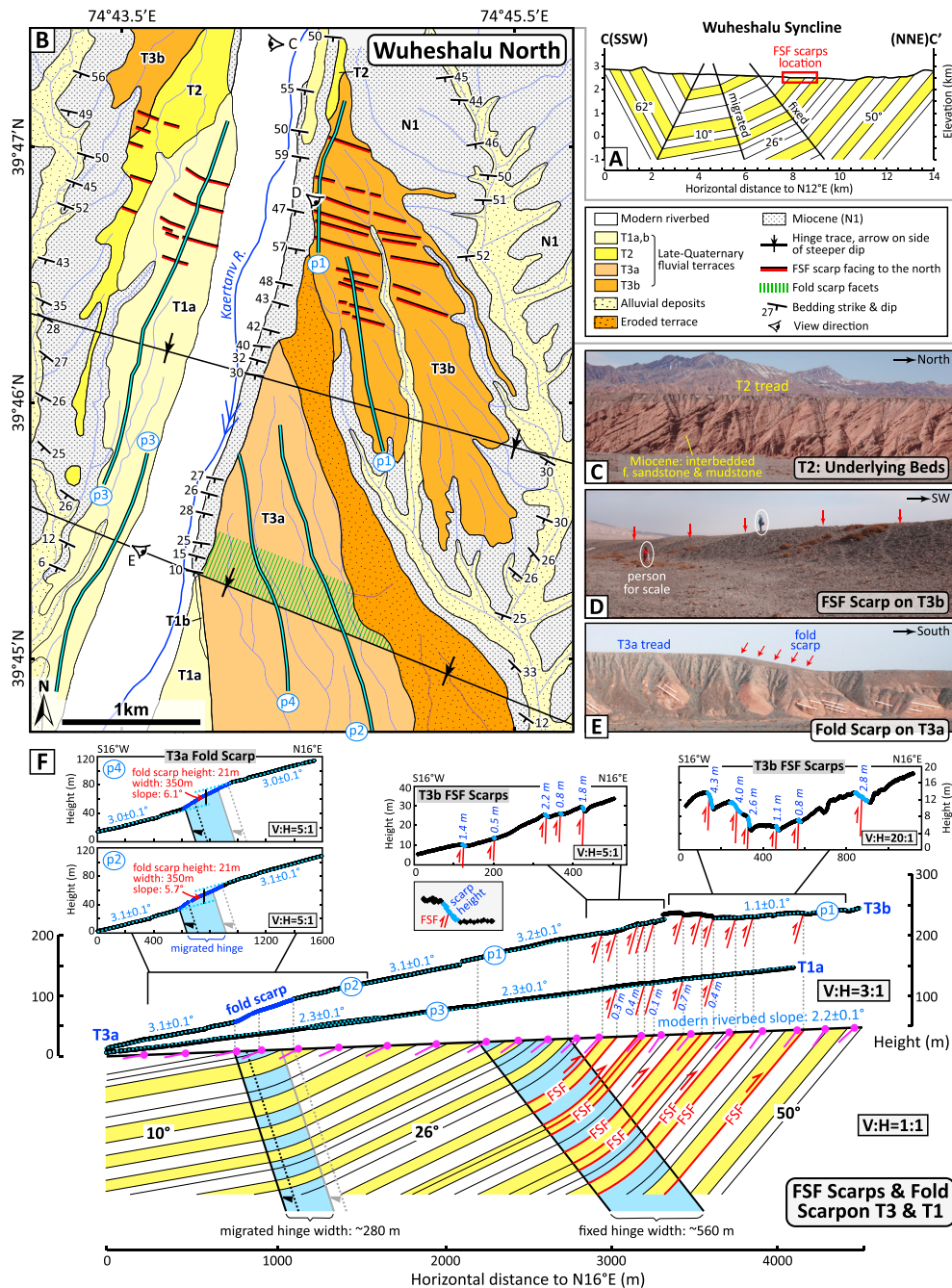
**Figure 7.** (a) Geologic and geomorphic map of Kalangoulvke River terraces at Kelatuo. Inset shows the Kelatuo cross section along the Kalangoulvke water gap. See Figure 2b for locations. (b) Photograph (viewpoint in Figure 7a) of a FSF scarp (red arrows) on the T3a tread and lower Miocene strata comprising interbedded fine sandstone and mudstone. (c) Topographic survey profile of active FSF scarps. See Figure 7a for the profile location. (d) Correlation of flexural slip surfaces (the fault number is correlated with that in Figure 7c) with bed lithology. The average thicknesses of sandstone and mudstone are ~2.3 and 6.3 m, respectively. See Figure 7a for the section location.

with this water gap, the fold geometry changes significantly: the eastern half trends east and is relatively open and broad, compared to its western half where the fold axis rotates to SE trending and becomes tight and narrow in response to the northward impingement of the Pamir Frontal Thrust.

Structural mapping along the Kaertanv water gap (transect C-C′; Figures 2b and 8a) defines an ~50°S dipping northern limb and an ~62°N dipping southern limb that are separated by a relatively broad hinge zone. Farther south, the fold is cut by the north vergent Pamir Frontal Thrust (Figure 2b). Lithified beds cropping out in the Wuheshalu fold include Paleogene through Pleistocene strata.

### 6.2. FSF Scarps and Terrace Deformation

In the Kaertanv water gap, fluvial terraces include three major groups (Figure 8b). As the most spatially extensive terrace, the T3 tread is separated into T3b and T3a sublevels by an ~20–30 m high eroded ridge. Beneath the capping fluvial deposits, the strata are characterized by interbedded thick mudstone and thin fine

**Figure 8.** (a) Cross section of the Wuheshalu syncline along the Kaertanv water gap and (b) geologic and geomorphic map of fluvial terraces at Wuheshalu northern limb. See Figure 2b for locations. (c–e) Photographs (viewpoints in Figure 8b) of lower Miocene beds exposed on the T2 riser, and a FSF scarp (red arrows) and a fold scarp (red arrows) on the T3 tread. (f) Topographic survey profiles of T3 and T1a treads and their correlation with folded bed geometry. See Figure 8b for profiles location.

sandstone of the lower Miocene. Dip measurements along terrace risers and deeply incised gullies define, from north to south, three panels with unidirectional dips of ~50°S, 26°S, and 10°S (Figures 8b and 8f). These panels are connected by discrete synclinal hinges, and the northern and southern ones are loosely defined to be ~560 and 280 m wide, respectively. North of the northern hinge, a suite of north facing FSF

scarps, with spacings of ~14–194 m, cuts the fluvial terraces (Figures 8b and 8d). Fault scarp heights range from ~0.5 to 4.3 m on the T3b tread and from ~0.1 to 0.7 m on the younger T1a tread, displaying increased height with terrace age.

Topographic measurements of the T3 and T1a treads, as well as the modern riverbed, span all three dip panels (Figures 8b and 8f), thereby permitting an explicit analysis of the folding mechanism. Within the northernmost panel, the T3b tread is cut by multiple FSFs and displays a general slope of ~1.1°S. Stretching southward across the northern synclinal hinge, the tread remains almost planar with a constant slope of ~3.2°S, despite local disruption by FSF scarps. Farther south, a SE striking, 21 m high, and 350 m wide topographic scarp with a slope of ~5.7–6.1°S deforms the T3a tread (Figures 8b and 8f and Table 2). This scarp can be traced laterally on the T3a tread and is associated with and trends parallel to the southern synclinal hinge in underlying beds (Figures 8b and 8f). These features support interpretation of this scarp as a typical fold scarp created by hinge migration (Chen et al., 2007; Hubert-Ferrari et al., 2007; Li et al., 2015a), analogous to the fold scarp at Mingyaole. Because the hinge migration distance of ~80 m (calculated from formula (2)) is much smaller than the hinge width of ~280 m, the scarp slope of ~6° is smaller than the predicted slope maximum of ~15° (Table 2). At the southernmost portion of survey profile, the tread slope returns to ~3.1°S. Overall, beyond the gentle slope of ~1.1°S at the northernmost that is perturbed locally by the FSF scarps and the steep slope ~6°S generated by hinge migration, the T3 tread maintains an almost constant slope of ~3.1°S across three dip panels. For the T1a terrace, although displaced by FSF scarps and spanning across the migrated hinge, the tread has a constant slope of ~2.3°S (Figure 8f).

An ~4.5 km long survey profile of the Kaertanv riverbed serves as a reference to evaluate the amount of limb rotation recorded by the terraces. Given the estimated gradient of ~2.2°S (Figure 8f), the T1a appears to be slightly tilted ~0.1°, whereas the T3 tread has a significant slope increase of ~1.0° (Table 2). According to formula (1), the ~50°S dip panel has rotated ~2.4° and 0.3° since abandonment of the T3 and T1a treads, respectively, implying the mechanism of limb rotation. Therefore, in addition to flexural slip and hinge migration, significant limb rotation contributes to the folding deformation at Wuheshalu.

## 7. Active Flexural-Slip Faulting at Wulagen

### 7.1. The Wulagen Syncline

The Wulagen syncline deforms the northern margin of the Mayikake basin (Figure 2b), a small-sized intramontane basin in the Pamir-Tian Shan convergent zone. The fold extends for ~10 km along the Kezilesu River and terminates close to the western end of the Kelatuo anticline. At the core of the fold, the north flowing Biertuokuoyi River and south flowing Kangsu River join with the Kezilesu River, which obscures bed outcrops and produces suites of fluvial terraces.

The Wulagen northern limb is well exposed. Along the Kangsu water gap (transect D-D′; Figures 2b and 9a), this limb is dominated by a geometrically simple, subvertical monocline comprising Miocene-Pliocene sandstone and Pleistocene conglomerate up to ~5–6 km thick. Comparatively, the core and southern limb are almost completely buried by fluvial deposits. Although detailed structural mapping is impractical, scattered Pleistocene outcrops in deeply incised gullies roughly define a broad hinge, across which the bed gradually changes from 80 to 86°SW dips in the north to dips of ~40°NE in the south (Figure 9a). The south vergent Mayikake Thrust, bounding the southern limb, creates east trending, south facing fault scarps on the surface (Figure 9b). Due to a lack of well-exposed bed outcrops and subsurface data, the subsurface geometry of this thrust and its geometric relationship with the Wulagen syncline cannot be determined.

### 7.2. FSF Scarps and Terrace Deformation

At Wulagen, three sets of terraces record recent folding-related deformation (Figure 9b). Among them, the T3 tread, which was emplaced near the end of the Last Glacial Maximum stage, is the most prominent and continuous (Li et al., 2012). This terrace can be subdivided into T3b and T3a: the former, older is ~4–5 m higher than the latter. In spite of the slight height difference, these two sublevels probably have different origins, based on interpretations from Google Earth© images. On the terrace T3a, the size and orientation of the fossil gravel bars preserved on the surface are parallel to those in the modern channel of the Kezilesu River, implying a consequent origin of the Kezilesu River. On the terrace T3b, however, the size and orientation of the fossil gravel bars correspond to the active ones of the Biertuokuoyi channel, and, therefore, it was likely
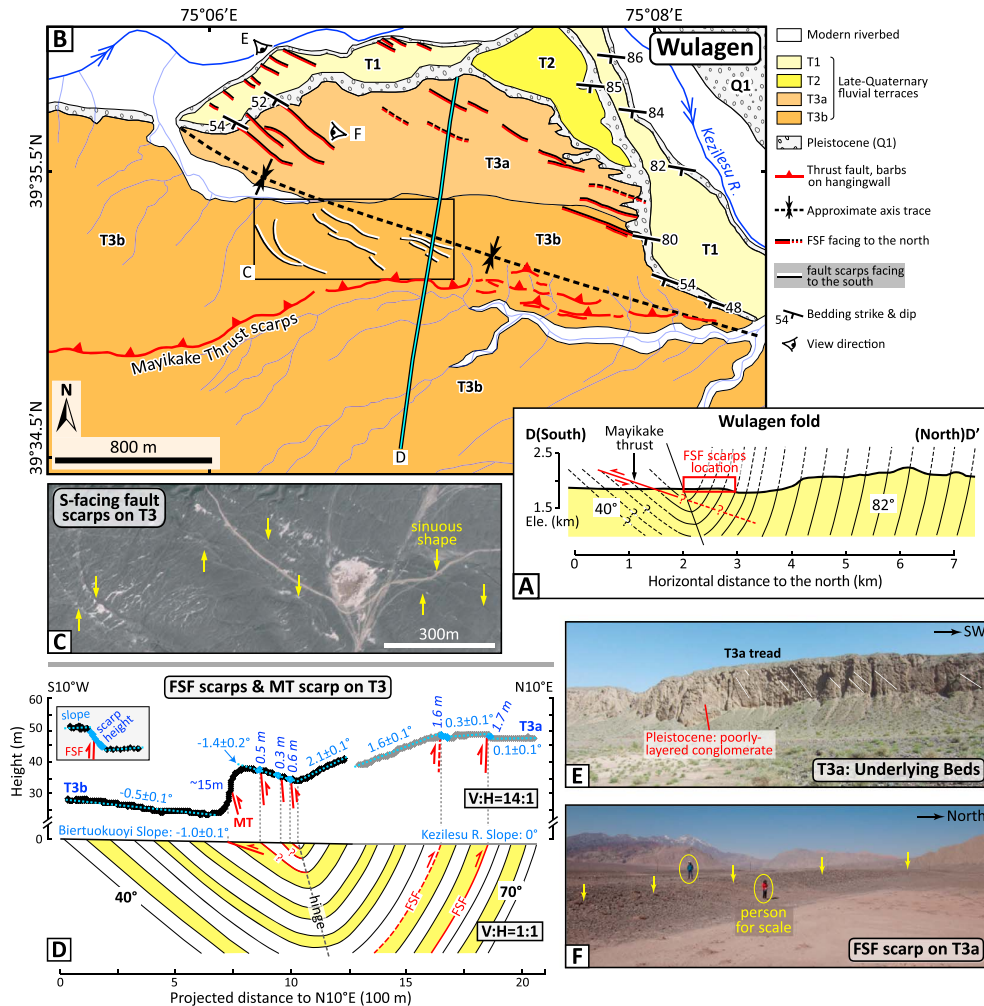
**Figure 9.** (a) A cross section of the Wulagen syncline and (b) geologic and geomorphic map of Wulagen fluvial terraces. The Mayikake Thrust (MT) on the Wulagen southern limb has a near-surface dip of 15–18° measured from fault outcrops (Li et al., 2012). The fault orientation at depth and its geometric association with the Wulagen fold are unknown. See Figure 2b for locations. (c) A Google Earth image illustrates that the south facing fault scarps on the T3b tread have more sinuous shape than FSF scarps at other sites. (d) Topographic survey profile of T3 tread and its correlation with folded bed geometry. Note that whether or not the south facing scarps are FSF scarps cannot be determined. See Figure 9b for the profile location. (e and f) Photographs (viewpoints in Figure 9b) of Pleistocene conglomerate exposed on the T3a riser and a FSF scarp (yellow arrows) on the T3a tread. Figures 9a–9d modified from Li et al. (2015b).

created by the Biertuokuoyi River. The bed underlying the fluvial terraces is dominated by massive, poorly layered Pleistocene conglomerate (Figure 9e).

One group of FSFs displaces, south-side-up, the T3 and T1 treads with scarp spacings of ~60 to 360 m and heights of ~0.3 to 4.2 m (Figures 9b, 9d, and 9f). These scarps trend ~40°SE in the west and rotate gradually eastward to ~70°SE and are located at the northern side of the synclinal hinge (Figure 9b). South of the hinge, the other group of fault scarps displaces the T3b tread (Figures 9b and 9c). These scarps are north-side-up and generally small, with spacings of ~23 to 73 m and heights of only ~0.3 to 0.6 m. Although subparallel with the northern FSF scarps, these scarps are far less linear (Figure 9c): somewhat inconsistent with the typical shape of FSF scarps. One possibility is that these scarps remain to be produced by flexural slip, and the sinuous fault scarps may be ascribed to the low magnitude of slip: when the fault localized along bed planes cuts through overlying fluvial deposits, the fault dip can change significantly if the slip amount is very low. The varying fault dips can result in a sinuous topographic scarp on the land surface. On the other hand,

these scarps could be produced by some kind of localized internal deformation, such as bending-moment reverse faulting (Yeats et al., 1997), instead of flexural slip. Due to this uncertainty, these scarps have not been analyzed in the subsequent discussion. At two sides of the hinge, the T3 tread slopes in opposite directions (Figure 9d): the southern segment slopes ~1.4°N, whereas the northern segment slopes get progressively more gentle: decreasing from ~2.1° to 1.6°S, and then decreasing from 0.3° to 0.1°S farther away from the hinge, thereby exhibiting a broad, upward, overall concave shape.

To evaluate whether or not limb rotation has occurred, the initial terrace slope should be determined. Because the T3b tread was created by the Biertuokuoyi River, its modern fluvial gradient of ~1.0°N is considered to represent its initial slope (Figure 9d). For the T3a tread that was created by east flowing Kezilesu River, the initial gradient in the north direction can be presumed to be ~0°. Relative to these two slopes, the T3 southern and northern segments on the hanging wall are, respectively, tilted ~0.4° and back-tilted 0.1–3.1° (to the south: opposite to the initial terrace slope), implying significant limb rotation of underlying ~40°N and 70°S dip panels. Given the broad curved hinge zone of the Wulagen fold (Figures 9a and 9d), inconsistent with the requirement of formula (1) as derived from a kink-style hinge geometry (see Appendix A), the limb rotation angle has not been estimated. However, the rotation angle is expected to be >0.1–3.1° as it is commonly higher than the terrace tilt (Figure 3a). Rotations of these two dip panels may be caused by tightening of the Wulagen syncline, by the curving and listric fault plane of the Mayikake Thrust (the fault plane with gradually changing dip will rotate the bed on the hanging wall; Amos et al., 2007), or by some combination of both.

## 8. Active Flexural-Slip Faulting at Biertuokuoyi

### 8.1. The Biertuokuoyi Frontal Thrust

Delineating the southwestern margin of the Mayikake basin, the Biertuokuoyi Frontal Thrust (BFT) is a lateral ramp of the Pamir Frontal Thrust (Figure 2b). The fault places Paleogene beds over uncemented Quaternary fluvial gravels along an ~75°SW dipping plane and creates a series of topographic scarps on the surface. Although no lateral offset of geomorphic markers has been detected, slickenlines with a rake of ~34° on the fault plane imply a high ratio of strike-slip to dip-slip motion (Li et al., 2012). The Biertuokuoyi Frontal Thrust plays an important role in regional shortening accommodation, and its Holocene dip-slip and total-slip rates are estimated to be ~2.9 and 3.6 mm/a, respectively (Li et al., 2012).

On the Biertuokuoyi hanging wall (Figure 2b), the fault activity exposes a succession of Paleogene and Miocene strata that are unconformably overlain by ~3000 m thick, Plio-Pleistocene piggyback basin sediments, representing syntectonic deposition related to the Pamir Frontal Thrust (Thompson et al., 2015). The bed continues to dip to the southwest, and its dip angle decreases gradually from ~62° to 50°, 30°, and 0° in the upstream direction of the Biertuokuoyi River (transect E-E'; Figures 2b and 10a), exhibiting a monocline composed of ~5–7 km thick Cenozoic unit (Figure 10a).

### 8.2. FSF Scarps and Terrace Deformation

Along the Biertuokuoyi River ~5–10 km southwest of the Biertuokuoyi Frontal Thrust, four sets of fluvial terraces were beveled into the Miocene bedrock of the hanging wall. The terrace treads T4 through T2a are marked by a SE trending, gently sloping topographic scarp (Figures 10b and 10d). This scarp displays increasing heights and widths with higher, older terrace levels, and its trend is parallel with the strike of underlying beds (Thompson, 2013). Although no beds crop out to the south of this scarp, dip data projected along strike from a transect ~4 km to the east indicate that a synclinal hinge can be projected along strike to coincide with this scarp. Across the hinge, the bed dip changes from ~62° to 50°SW. Based on these observations, we interpret this scarp as a fold scarp formed by migration of the synclinal hinge, analogous to fold scarps at Mingyaole and Wuheshalu. On the northern T4 and T3 treads that overlie the ~62°SW dip panel (Figures 10b–10d), a group of FSF scarps is present with heights of ~0.1 to 0.5 m. Despite low heights, tan ponded deposits at the front of those scarps and significant NW trending linear features make them apparent from the topographic noise of the terrace surface. More than 10 FSF scarps have been detected to occur in an ~600 m wide zone and space in a range of ~12 to 103 m. All FSF scarps are restricted to the fold scarp slope: a contrast to the Mingyaole FSF scarps that commonly occur on the upper tread above the scarp (Figures 4–6).
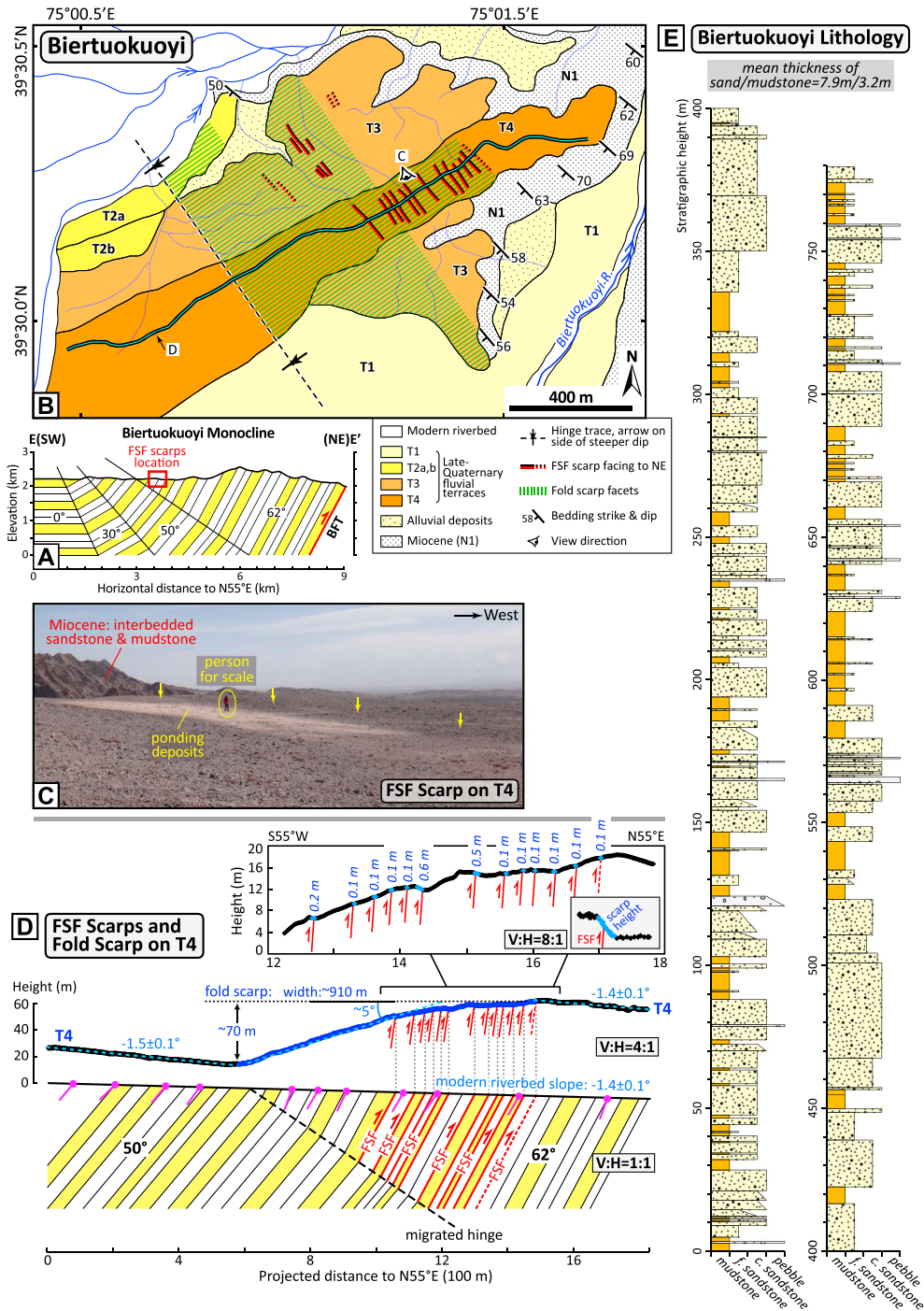
**Figure 10.** (a) Cross section of the Biertuokuoyi monocline and Biertuokuoyi Frontal Thrust (BFT) along the Biertuokuoyi water gap and (b) geologic and geomorphic map of fluvial terraces. Top and foot of the fold scarp are located from topographic survey profiles (Thompson, 2013), so that its spatial extent on T4, T3, and T2a terraces can be roughly defined. See Figure 2b for locations. (c) Photograph (viewpoint in Figure 10b) of a FSF scarp (yellow arrows) on the T4 tread. (d) Topographic survey profile of the T4 tread correlated with folded bed geometry. See Figure 10b for the profile location. (e) The bed lithology at Biertuokuoyi. The average thickness of sandstone and mudstone are ~7.9 and 3.2 m, respectively. Because the section (see Figure 2b for the location) crops out too far away from the FSF scarps, the correlation between specific stratigraphic levels and flexural-slip surfaces has not been carried out.

In order to determine the amount of limb rotation, we measured the T4 tread, the best preserved and most laterally extensive terrace at this site (Figures 10b and 10d), as well as the modern riverbed to the northwest of the terraces. With a height of ~70 m and a width of ~910 m, the fold scarp slopes ~5°SW (Figure 10d), compatible with the predicted slope maximum of ~4–5° (Table 2), implying that the hinge migration distance exceeds the hinge width and the fold scarp has already approached the maximum slope. The upper and lower treads bounding the fold scarp have similar slopes of 1.4 ± 0.1°NE, close to the modern riverbed slope of ~1.4°NE, providing an indication of negligible amount of terrace tilt and limb rotation. Hence, deformation at Biertuokuoyi is dominantly achieved by hinge migration and flexural slip (Figure 1b).

The upper Miocene strata beneath terrace deposits cannot be traced continuously to the south of the fold scarp. We logged an ~780 m thick section ~4 km southeast of the mapping area to explore the bed lithology (Figure 10e). The result reveals the beds characterized by thick sandstone and thin mudstone with average bed thicknesses of ~7.9 and 3.2 m, respectively.

## 9. Active Flexural-Slip Faulting at Bashjiqike

Now let us focus on the Kuche fold belt, ~700 km northeast along the southern Tian Shan piedmont from the Pamir-Tian Shan convergent zone (Figures 2a and 2c). Although the Kuche fold belt also includes an array of active folds, such as the Quilitage and Yaken anticlines along the leading edge (Hubert-Ferrari et al., 2007; Saint-Carlier et al., 2016), FSF scarps have only been detected in the Bashjiqike anticline, lying in the northernmost part of the fold belt. This limited occurrence contrasts strongly with the widespread presence of FSF scarps in the Pamir-Tian Shan convergent zone.

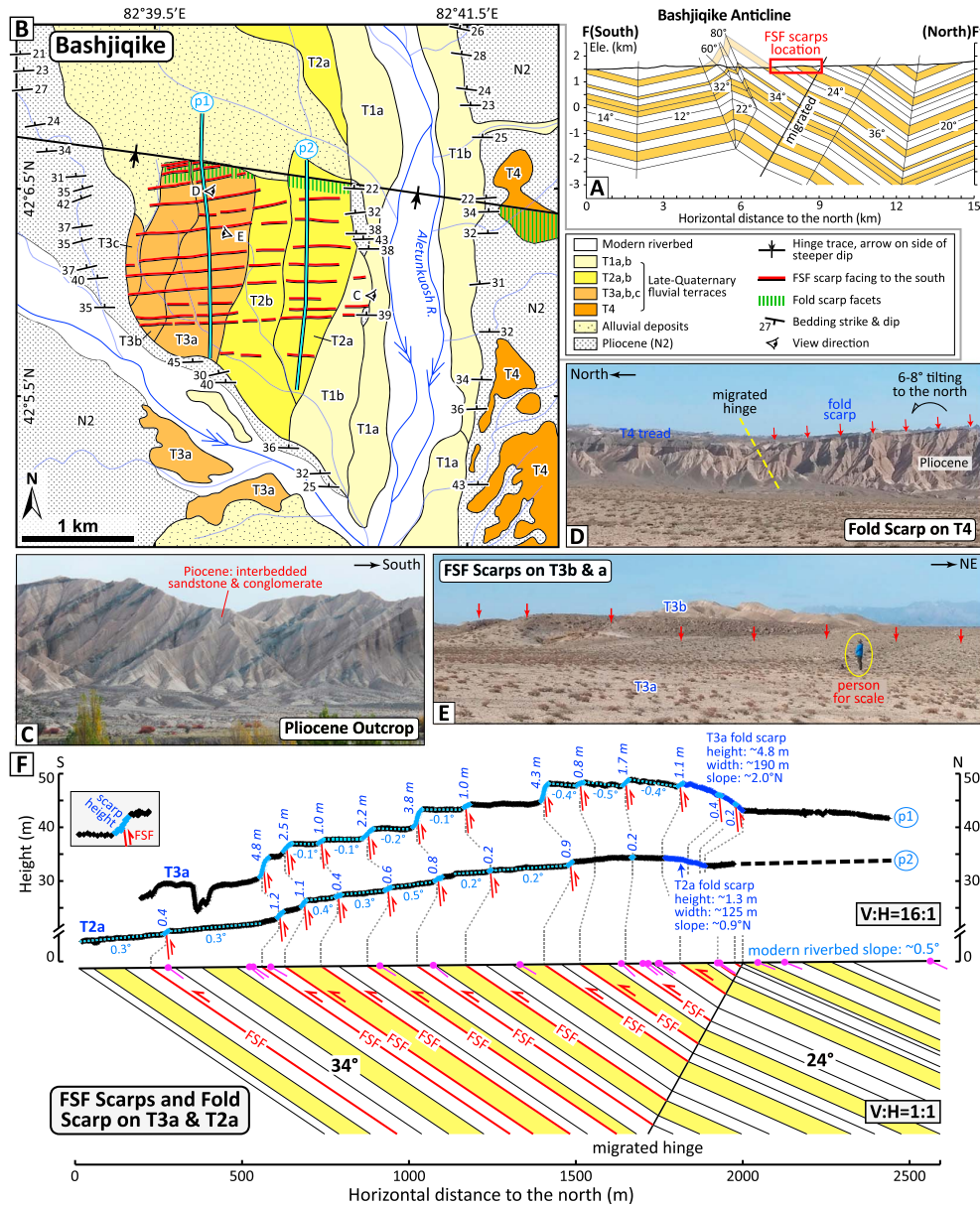### 9.1. The Bashjiqike Anticline

Along the southern Tian Shan piedmont (Figure 2c), the Bashjiqike anticline is a rugged and largely mountainous ridge that extends for ~70 km between the Kumugeliem anticline to the west and the Kuche River to the east. The transverse Aletunkuosh River and Kuche River, with headwaters in the southern Tian Shan mountains, deeply incise into the ridge and then flow south into the Tarim basin.

The fold exposes lithified Mesozoic through Miocene units in its core and Plio-Pleistocene units on its two limbs (Figure 2c). The cross section along the Aletunkuosh water gap depicts an asymmetric fold with a broad, 24–36°N dipping northern limb; a narrow, 32–80°S dipping southern limb; and a tight core composed of several highly deformed secondary folds (Figure 11a, see Figure 2c for the section location). As interpreted from a seismic profile close to the water gap (Figure 8 in Wang et al., 2011), the fold is probably a fault-propagation fold controlled by a south vergent thrust ramp that is parallel with beds on the hanging wall (northern limb) and is rooted within the Paleogene detachment surface. Growth strata and an angular unconformity imaged on the seismic profile indicate that the fold initiated at the beginning of Miocene, only slightly younger than the latest uplift time of the southern Tian Shan (Wang et al., 2011). Farther south, the fold connects with the Kasangtuokai anticline through an open and broad syncline (Figures 2c and 11a).

### 9.2. FSF Scarps and Terrace Deformation

The Aletunkuosh River incises the Pliocene beds, which are characterized by interbedded thick, muddy sandstone and thin conglomerate, to create a number of fluvial terraces (Figure 11). Terraces at this site include more individual treads but are less spatially extensive compared with those in the Pamir-Tian Shan convergent zone. In our geomorphic mapping (Figure 11b), small, adjoining terraces with little vertical separation have been amalgamated into a single level, after that these levels have been divided into four major groups: terraces T4 to T1 elevate 70–90, 40–55, 30–36, and 0–20 m above the modern riverbed, respectively.

Underlying the fluvial terraces, a synclinal hinge separates two panels with unidirectional dips of ~24°N and 34°N (Figure 11f). Trending parallel with the hinge, a gentle back-sloping (to the north) topographic scarp is present on terraces T4 through T2. The height/width/slope of the scarp is ~4.8 m/190 m/2.0°N on the T3a and ~1.3 m/125 m/0.9°N on the T2a (Table 2). For the T4 fold scarp, the upper tread abutting the scarp was eroded and its topographic measurement was impeded because of inaccessibility. A measurement on the field photo approximates a slope of ~6–8°N relative to the terrace to the north of the hinge (Figure 11d). The association with the synclinal hinge and the increasing height and width with terrace age characterize this scarp as a typical hinge-migrated fold scarp (Figure 3b).

**Figure 11.** (a) Cross section of the Bashjiqike anticline along the Aletunkuosh water gap and (b) geologic and geomorphic map of fluvial terraces on the Bashjiqike northern limb. See Figure 2c for locations. (c–e) Photographs (viewpoints in Figure 11b) of the Pliocene beds, the fold scarp (red arrows) on the T4 tread, and the FSF scarp (red arrows) on the T3 tread. The ~6–8° tilting of the fold scarp (Figure 11d) measured on the photograph relative to the terrace to the north of the hinge. (f) Topographic survey profiles of T3a and T2a treads and their correlation with folded bed geometry. See Figure 11b for the profile locations.

According to the underlying bed dip change (Figure 11f), the fold scarp can approach a maximum slope of ~8° (Table 2). This slope is compatible with the T4 scarp slope but is much larger than those of the T3a and T2 scarps, indicating that the hinge migrated a distance exceeding the hinge width for the T4 terrace but migrated less than the hinge width for the T3a and T2a terraces. Because the underlying thrust ramp is parallel with the hanging wall beds, fault slip increments can be calculated from formula (4) to be ~31 and ~9 m since abandonment of the T3a and T2a terraces, respectively. The terrace age has not been determined; however, existing dated terraces in the Pamir and Tian Shan regions indicate that spatially extensive
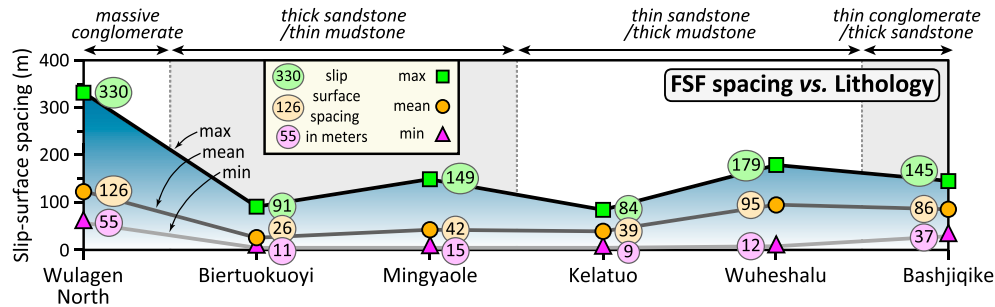
**Figure 12.** The maximum, mean, and minimum slip-surface spacing as a function of lithology at Wulagen North, Biertuokuoyi, Mingyaole, Kelatuo, Wuheshalu, and Bashjiqike. Note that the spacing in the conglomerates at Wulagen North is much larger than that at other sites.

strath terrace formation is typically climatically controlled, and terraces are most commonly abandoned during glacial-interglacial transitions (e.g., Huang et al., 2014; Li et al., 2013; Lu et al., 2010; Molnar et al., 1994; Pan et al., 2003). If we assign an age of ~15 ka (transition from Marine Isotope Stages 2 to 1; Lisiecki & Raymo, 2005) to the T2 terrace (similar to the age of terrace T3 at Kalangoulvke South and terrace T3 at Wulagen), the slip rate of the thrust controlling the Bashjiqike fold is estimated to be ~0.6 mm/a.

Compared with the low and gentle fold scarp, the FSF scarps are more visually conspicuous (Figures 11b, 11d, and 11e). About 14 north facing FSF scarps are distributed across an ~1700 m wide zone with spacing ranging from 14 to 190 m. The scarp height varies from 0.2 to 4.8 m on the T3a tread and from 0.2 to 1.2 m on the T2a tread (Figures 11f). On the T3 tread, with the exception of four relatively low scarps on the scarp slope, the majority lies to the south of the fold scarp. Because of strong displacement of FSFs, the slope and tilt of the terrace tread cannot be well determined. However, the terrace segment on the hanging wall of each fault displays roughly constant slopes of 0.1–0.5°N for the T3a tread and 0.2–0.5°S for the T2a tread (Figure 11f and Table 2). With respect to the modern fluvial gradient of ~0.5°S (Figures 11f), most terrace segments of T3a and T2a appear to be back tilted (to the north), implying some degree of rotation of the underlying ~34°N dip panel. Overall, in addition to hinge migration, the folding deformation at Bashjiqike is probably contributed by certain limb rotation as well (Figures 1 and 3).

## 10. Discussions

Data collection of significant flexural-slip fault (FSF) scarps, well-preserved terrace treads, and well-exposed folded bedrock at eight new sites provides a uniquely broad basis for analyzing and summarizing the conditions that favor the development of FSF scarps, including bed lithology and dip, slip-surface spacing, and folding mechanism. We sequentially discuss the controls exerted by each of these parameters.

### 10.1. Lithology

In previous studies (e.g., Davis et al., 2012; Tanner, 1989; Tavani et al., 2015), a proposed prerequisite for flexural slip is that the bed has a strong mechanical anisotropy. A well-layered sedimentary succession made of competent, for example, conglomerate, sandstone, and carbonate, alternating with incompetent beds, for example, siltstone, mudstone, and shale, is postulated to facilitate flexural slip. Conversely, in massive beds made of thick, poorly layered strata, flexural slip is likely to be inhibited.

The bed lithology changes significantly across our study sites (Figure 12). At Mingyaole and Biertuokuoyi (Figures 4d, 5d, and 10e), the beds comprise relatively thick sandstone (mean thickness of ~6–8 m) alternating with thin mudstone (mean thickness of ~3–4 m) of upper Miocene-Pliocene age. At Kelatuo and Wuheshalu (Figures 7d and 8c), the beds are characterized by interbedded thin fine sandstone and thick silt-mudstone of lower Miocene age. At Bashjiqike (Figure 11c), the beds are dominated by interbedded thick muddy sandstone and thin conglomerate of Pliocene age. The lithologies at these sites are consistent with the purported requirement for strong mechanical contrasts to promote flexural-slip faulting. As pointed out by Ramsay (1967) and Tanner (1989), mechanical contrasts between distinct lithologies can strongly control the location of flexural slip surfaces as well. Our stratigraphic logs at Mingyaole South and Kelatuo (Figures 4d, 5d, and 7d) document this point again: despite two slip surfaces at Kelatuo that occur in thick
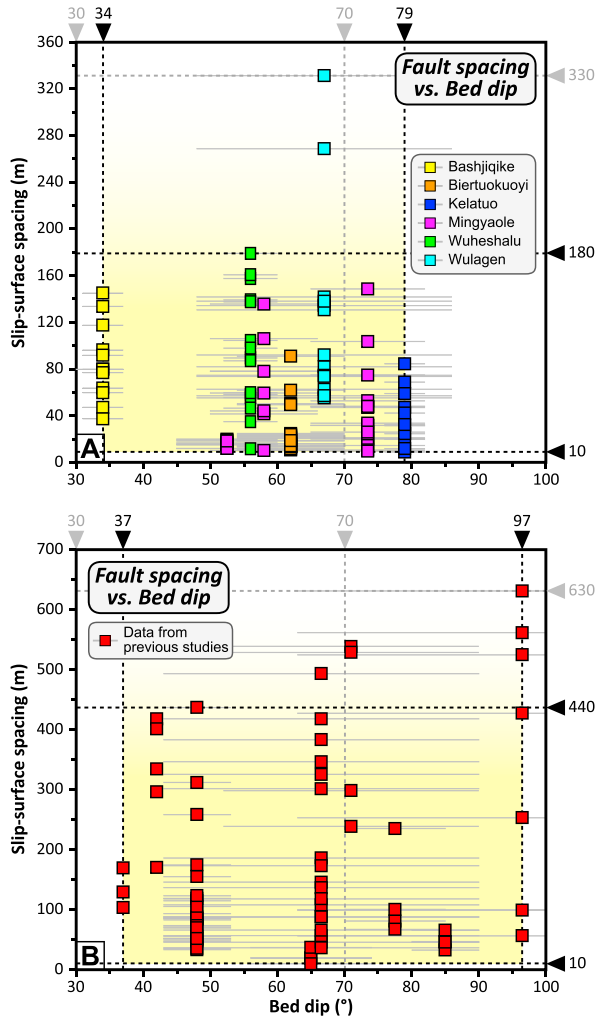
**Figure 13.** Statistical analyses of slip-surface spacing and underlying bed dip of FSF scarps based on data from (top) eight sites in this study and (bottom) nine sites in previous studies (Table 1). The slip-surface spacing is commonly defined as ~10–440 m but can reach up to ~630 m. The bed dip ranges from ~34 to 97° (some dips larger than 90° because of overturned beds).

mudstone layers, all others occur either (i) close to (<1.0 m) or along the sand/mudstone (competent/incompetent) contacts or (ii) within mudstone (incompetent) layers as thin as ~0.6–2.8 m.

An exception occurs at Wulagen, where FSF scarps are still clearly present in spite of the massive Pleistocene conglomerate (Figure 9e), indicating that a strong mechanical contrast is not wholly necessary. Although flexural slip faulting commonly operates in well-layered beds, such faulting can also develop uncommonly in massive, poorly layered beds.

### 10.2. Bed Dip

An interesting observation in this study is that FSF scarps seem to always be present overlying the steepest beds at each fold limb. For instance, the bed dip of Wuheshalu northern limb decreases from ~50° to 26° and 10° to the south, and FSF scarps are only present in the ~50° dip panel (Figure 8). Similarly, Mingyaole FSF scarps are restricted in the steepest ~50–58° dip panel and ~70° dip panel on the southern and northern limbs, respectively (Figures 4–6). This restriction to steeply dipping panels suggests that development of FSF scarps strongly depends on the presence of underlying steep beds.

In light of observations in both bed outcrops and analog modeling (Behzadi & Dubey, 1980; Gutiérrez-Alonson & Gross, 1999; Ramsay, 1974), bed dips of ~30–70° may be the most mechanically favorable to focus flexural slip: during progressive folding, flexural slip is negligible before the bed reaches an ~30° dip and then increases rapidly until it almost ceases at a dip of ~60–70° due to both increasing frictional resistance between beds and locking up of the slip surface.

Statistical analysis of 17 sites in our current and previous studies shows that all FSF scarps are present overlying bed dips of ≥34° (Figure 13 and Table 1), in agreement with the minimum dip of ~30° in previous determinations. The maximum bed dip that accommodates FSF scarps, however, can significantly exceed the expected ~60–70° and can even exceed ~90° (Figure 2 in Yeats et al., 1981 and Figure 24 in Philip & Meghraoui, 1983; the bed dip larger than 90° because of the bed overturning), significantly exceeding the expected maximum dip of ~60–70°. The reason for this large discrepancy is unknown. A speculative one, as suggested by Gutiérrez-Alonson and Gross (1999), is that initial development of flexural slip will cease once the critical dip of ~60–70° is reached, but displacement and propagation of other types of secondary faults (e.g., bending-moment faults) may unlock the slip surface and thus permit their subsequent reactivation (Figure 12 in Gutiérrez-Alonson & Gross, 1999).

### 10.3. Slip-Surface Spacing

The presence of FSF scarps is also controlled by the spacing of viable slip surfaces. On the one hand, for a given fold deformation, flexural slip amount is proportional to the slip-surface spacing (Davis et al., 2012; Ramsay, 1967), and only surfaces spaced widely enough can generate sufficient slip to produce a recognizable topographic expression. Meanwhile, the spacing cannot be too large; otherwise, the lack of slip surfaces will prohibit the mechanism of flexural slip, which will be overridden by the development of other types of secondary faults, for example, bending-moment faults (Tavani et al., 2015). A summary of our and previous studies suggests that the slip-surface spacing (calculated by map-view spacing of FSF scarps multiplied by sine of the average bed dip which presumably represents the dip of the fault plane) is generally ~10–180 m or ~10–440 m, respectively, but can reach as high as ~630 m (Figure 13). We propose the most appropriate slip-surface spacing for FSF scarps to be ~10–440 m, approximately 2 to 3 orders of magnitude larger

than that typical of FSFs in well-bedded outcrops (several centimeters to meters) (Horne & Culshaw, 2001; Tanner, 1989).

According to Tanner (1989) and Tavani et al. (2015), the slip-surface spacing is influenced by lithology: closer spacing is expected in well-layered beds, whereas wider spacing should dominate in a sequence containing massive or internally cemented beds. This contention is, to some extent, supported by our observation at Wulagen North (Figure 12), where statistical analysis of the maximum, average, and minimum slip-surface spacing at each site shows that the spacing at Wulagen North, where the bed lithology is dominated by massive conglomerate, is much larger than that at other sites characterized by well-layered beds. Although the bed lithology at Biertuokuoyi, Mingyaole, and Bashjiqike is much coarser than that at Kelatuo and Wuheshalu (Figure 12), the spacing shows similar ranges, implying that favorable positions for the slip surface are independent of grain size.

### 10.4. Folding Mechanisms

The flexural-slip faulting models in Figure 1 (refer to Shaw et al., 2005 and Tavani et al., 2015) illustrate that FSF scarps can be distributed across an entire rotating limb but are commonly restricted to the slope of the hinge-migrated fold scarp. These contrasting distribution characteristics can be applied to evaluate contributions of limb rotation and hinge migration to flexural slip. According to our eight study sites (Table 1), with the exception of Kelatuo where the folding mechanism cannot be determined, the Wuheshalu, Wulagen, and Bashjiqike are dominated or partially contributed by limb rotation, whereas the other four sites, including Caijinchang, Kalangoulvke South and North, and Biertuokuoyi are dominated by hinge migration with unclear limb rotation. Integration of our eight sites with 12 sites from previous studies yields a total of 20 sites: five limb-rotation-contributed sites (three in this study), seven hinge-migration-dominated sites (four in this study), and eight sites with an unknown folding mechanism (one in this study). For all five limb-rotation-contributed sites, for example, Wulagen and Bashjiqike (Figures 9b and 11b), FSF scarps are widely distributed on the rotating dip panel, consistent with the model prediction in Figure 1a.

An unexpected result from seven dominantly hinge-migration sites is that, except Biertuokuoyi FSF scarps that seem to be totally restricted to the slope of the fold scarp (Figure 10), most or all of FSF scarps at other sites occur in a wide zone beyond the fold scarp. For example, at Kalangoulvke South and North (Figures 5 and 6), all FSF scarps occur in a zone as wide as ~800–1000 m on the upper tread beyond the fold scarp. At Caijinchang (Figure 4), only one to two FSF scarps are found on the fold-scarp slope, whereas the majority is present to the north of the fold scarp. These observations contradict the model prediction in Figure 1b. One explanation is that weak limb rotation that is undetectable in our topographic survey data accounts for the folding deformation, thereby producing clearly expressed FSF scarps at these sites. The other possibility comes from our basic assumption (section 3.2): the modern riverbed gradient is used to represent the initial slope of all fluvial terraces. This assumption brings about some uncertainty in the assessment of limb rotation, because the fluvial gradient may change due to sediment or water discharge variations and base level changes. For example, if the initial slope is much smaller than the modern fluvial gradient of ~1.0°S, the Kalangoulvke South T3 tread would have experienced significant limb rotation. Whether or not the mechanism of limb rotation is weak or significant, if the basic FSF model in Figure 1 is valid, some rotation seems required to explain FSF scarps located beyond the fold scarp. Given available data where the folding mechanism is well determined and the distribution characteristics of FSF scarps are clear, we speculate that FSF scarps are dominantly generated in conjunction with limb rotation. Compared to hinge migration, limb rotation is generally required to produce significant topographic scarps.

### 10.5. Other Potential Controlling Factors

The bed lithology and dip, slip-surface spacing, and the mechanism by which folding occurs may be the most important controlling factors of active flexural-slip faulting. However, the influence of several potentially important factors remains unresolved. One is the folding rate: is it easier to produce FSF scarps with a higher rate of limb rotation or hinge migration? This factor has not been evaluated in this study, because folding rates at each site are not well constrained. Another factor may be the regional convergent rate. In fact, the widespread occurrence of both numerous and clear FSF scarps in the Pamir-Tian Shan convergent zone appears unusual, compared to only a single site with FSF scarps in Kuche fold belt. Furthermore, FSF scarps are rarely identified in other similar tectonic settings, such as the Kepintagh fold belt at the middle of the

Pamir-Tian Shan convergent zone or the Hetian fold belt ~400 km to the southwest of the Pamir-Tian convergent zone, where our field surveys, observations of high-resolution Google Earth imagery, and previous studies have failed to distinguish widespread and clear FSF scarps. A possible cause for such differences may be the high convergent rate of ~7–11 mm/a in the Pamir-Tian Shan convergent zone, a zone <100 km in width (Li et al., 2012; Yang et al., 2008; Zubovich et al., 2010), much higher than the rate at other three sites (Figure 2a). Although the straightforward cause and effect are unclear, the high rate can increase the number of active and strongly deforming folds, uplift more lithified and well-layered bedrock, and increase the deformation rate of individual folds, all of which can increase opportunities and contribute to produce FSF scarps.

A final consideration is the development of geomorphic surfaces. The occurrence of FSF scarps requires not only conditions that facilitate accumulation of flexural slip but well-developed geomorphic surfaces to record such scarps. FSF scarps are most recognizable in arid areas dominated by wide and continuous terraces, rather than narrow, vegetated, and locally preserved terraces that are more likely to be dissected by channels or covered by trees or colluvium. This point can be well manifested by distribution of identified FSF scarps in the Pamir-Tian Shan convergent zone (Figure 2b): six sites of FSF scarps are located to the east of the Mayikake basin, where the Kezilesu River and its tributaries create flights of laterally extensive and well-preserved fluvial terraces (Figures 4–7 and 9 and 10), compared to only one site of FSF scarps to the west of the Mayikake basin, where the area is dominated by exposed lithified beds, instead of well-developed fluvial terraces (Figure 2b). In addition, old terraces capped by thin fluvial deposits are expected to favor more clear surface expression of flexural slip than young terraces capped by thick fluvial deposits.

## 11. Conclusions

Numerous, clearly expressed flexural-slip fault (FSF) scarps and well-exposed underlying folded beds in the Pamir-Tian Shan convergent zone, NW China, permit a detailed investigation of the conditions favoring active flexural-slip faulting. Our study indicates the following:

1. Flexural slip commonly operates in well-layered beds, although such slip can occur in massive, poorly layered beds as well.
2. The slip surface is commonly located either (a) close to (<1.0 m) or along contacts of competent and incompetent beds or (b) within thin incompetent beds.
3. FSF scarps are always found overlying steep beds with dips larger than ~30°, but less than ~100°.
4. Slip-surface spacing is likely to be in a range of ~10–440 m but can reach up to ~600 m. In poorly layered beds, the slip-surface spacing is wider than that in well-layered beds.
5. FSF scarps are dominantly generated in conjunction with limb rotation. Compared to hinge migration, limb rotation is generally required to accumulate large amounts of flexural slip and produce easily recognizable topographic scarps.
6. A region with a higher convergent rate seems to have more opportunities of creation of FSF scarps than a region with a lower convergent rate. Meanwhile, a region dominated by well-preserved, old, and thin deposit-capped terraces is expected to record more clear FSF scarps than a region dominated by only locally preserved, young, vegetated terraces capped by thick fluvial deposits.

Even though the above conditions can be completely satisfied, FSF scarps may not necessarily be generated. Consider the Atushi anticline immediately to the east of the Kelatuo anticline, as an example (Figure 2b), the fold has similar bed lithologies as the nearby Kelatuo fold and steep limbs, as well as significant limb rotation (Heermance et al., 2008; Scharer et al., 2006). However, the folding accommodation is dominated by bending-moment faulting, instead of flexural slip (Heermance et al., 2008). The other example is from the Mingyaole anticline: the significant FSF scarps at Caijinchang and Kalangoulvke South cannot be traced laterally to its southwestern end where the bed has similar lithology, the bed dip is as large as ~46°, and the fold experiences strong limb rotation (Li et al., 2013). This contrast indicates that the fold growth might be accommodated by more diffuse deformation mechanisms, such as flexural flow (e.g., Davis et al., 2012). Why FSF scarps are present at one site but not at other sites in a similar geologic setting and even along the same fold? How do different accommodating mechanisms transit among each other? How does the rate of folding affect the style and abundance of flexural-slip faulting? Answers to these questions await more well-calibrated field studies, further investigations of other deformation mechanisms, and additional analog modeling.

### Appendix A: Geometric Relationship Between Limb Rotation and Terrace Tilting

We follow the limb rotation model proposed by Poblet and McClay (1996) and Poblet et al. (1997) to derive geometric relationship between terrace tilting and limb rotation. To simplify geometric calculations, (i) a kink-style hinge, instead of a curved hinge, is used to characterize the folded bed geometry and (ii) the hinge is pinned at the point "A" on the land surface (Figure A1). When the bed rotates $\phi'$ to increase its dip from $(\theta_2 - \phi')$ to $(\theta_2)$, the bed segment $BC$ will migrate from dip panel to the right of the hinge into dip panel $(\theta_1)$ to the left of the hinge because the hinge rotates $(\phi'/2)$. During this process, the bed length is conserved:
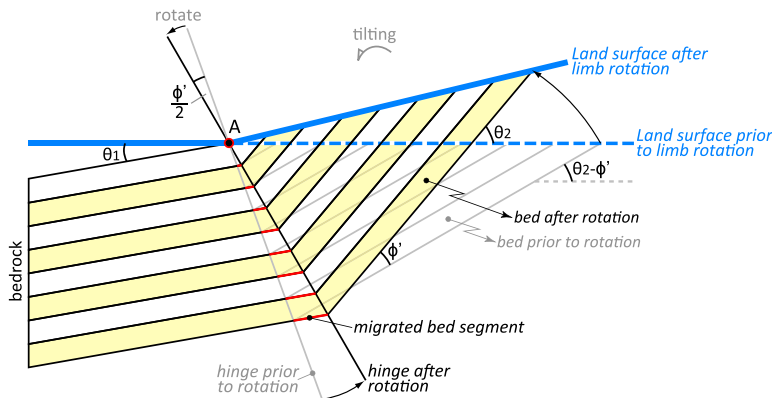
$$BC + CE = BD,$$

where $BD$ is the bed length before limb rotation and $CE$ is the length of bed segment dipping $(\theta_2)$ after limb rotation. According to trigonometric relationships illustrated in Figure A1, we have
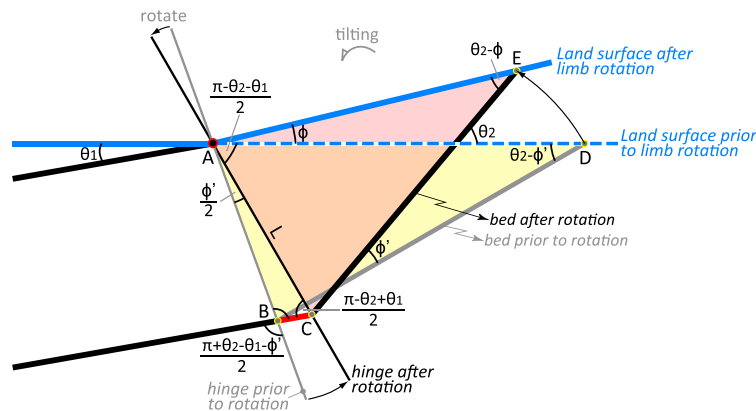
$$\frac{BC}{\sin\angle BAC} = \frac{AC}{\sin\angle ABC} \;\Rightarrow\; \frac{BC}{\sin\left(\frac{\phi'}{2}\right)} = \frac{L}{\cos\left(\frac{\theta_2-\theta_1-\phi'}{2}\right)} \;\Rightarrow\; BC = \frac{\sin\left(\frac{\phi'}{2}\right)}{\cos\left(\frac{\theta_2-\theta_1-\phi'}{2}\right)}L \tag{A1}$$

$$\frac{CE}{\sin\angle CAE} = \frac{AC}{\sin\angle AEC} \;\Rightarrow\; \frac{CE}{\sin\left(\frac{\pi-\theta_2-\theta_1}{2}+\phi\right)} = \frac{L}{\sin(\theta_2-\phi)} \;\Rightarrow\; CE = \frac{\cos\left(\frac{\theta_2+\theta_1}{2}-\phi\right)}{\sin(\theta_2-\phi)}L \tag{A2}$$



**Figure A1.** The geometric relationship of limb rotation and terrace tilting. (a) When the bed rotates to increase its dip from $(\theta_2 - \phi')$ to $(\theta_2)$, the bed segment (red lines) will migrate from dip panel to the right of the hinge into dip panel $(\theta_1)$ to the left of the hinge because the hinge rotates $(\phi'/2)$ around the point "A" that is fixed on the land surface. (b) Rotation of underlying bed $(\phi')$ and tilt of the land surface $(\phi)$ have a predicted geometric relationship.

$$\frac{BD}{\sin\angle BAD} = \frac{AB}{\sin\angle ADB} \quad \Rightarrow \quad \frac{BD}{\sin\left(\frac{\pi-\theta_2-\theta_1+\phi'}{2}\right)} = \frac{AB}{\sin\left(\theta_2-\phi'\right)} \tag{A3}$$

Because

$$\frac{AB}{\sin\angle ACB} = \frac{AC}{\sin\angle ABC} \quad \Rightarrow \quad \frac{AB}{\sin\left(\frac{\pi-\theta_2+\theta_1}{2}\right)} = \frac{L}{\sin\left(\frac{\pi+\theta_2-\theta_1-\phi'}{2}\right)} \quad \Rightarrow \quad AB = \frac{\cos\left(\frac{\theta_2-\theta_1}{2}\right)}{\cos\left(\frac{\theta_2-\theta_1-\phi'}{2}\right)}L,$$

if we put this formula into formula (A3), we have

$$BD = \frac{\cos\left(\frac{\theta_2+\theta_1-\phi'}{2}\right)\cos\left(\frac{\theta_2-\theta_1}{2}\right)}{\sin\left(\theta_2-\phi'\right)\cos\left(\frac{\theta_2-\theta_1-\phi'}{2}\right)}L \tag{A4}$$

Given that $BC + CE = BD$, we can obtain the tilt angle ($\phi$) of fluvial terrace according to formulas (A1), (A2), and (A4):

$$\tan\left(\frac{\theta_2+\theta_1}{2}-\phi\right) = \frac{\sin\left(\theta_2-\phi'\right)\cos\left(\frac{\theta_2-\theta_1-\phi'}{2}\right)}{\cos\left(\frac{\theta_2-\theta_1}{2}\right)\left[\cos\left(\frac{\theta_2+\theta_1-\phi'}{2}\right)\cos\left(\frac{\theta_2-\theta_1}{2}\right) - \sin\left(\theta_2-\phi'\right)\sin\left(\frac{\phi'}{2}\right)\right]} - \tan\left(\frac{\theta_2-\theta_1}{2}\right)$$

## References

Allen, M. B., Windley, B. F., & Chi, Z. (1999). Late Cenozoic tectonics of the Kepingtage thrust zone: Interactions of the Tien Shan and Tarim Basin, northwest China. *Tectonics*, *18*(4), 639–654. https://doi.org/10.1029/1999TC900019

Amos, C. B., Burbank, D. W., Nobes, D. C., & Read, S. (2007). Geomorphic constraints on listric thrust faulting: Implications for active deformation in the Mackenzie Basin, South Island, New Zealand. *Journal of Geophysical Research*, *112*, B03S11. https://doi.org/10.1029/2006JB004291

Avouac, J.-P., Tapponnier, P., Bai, M., You, H., & Wang, G. (1993). Active thrusting and folding along the northern Tien Shan and Late Cenozoic rotation of the Tarim relative to Dzungaria and Kazakhstan. *Journal of Geophysical Research*, *98*(B4), 6755–6804. https://doi.org/10.1029/92JB01963

Behzadi, H., & Dubey, A. K. (1980). Variation of interlayer slip in space and time during flexural folding. *Journal of Structural Geology*, *2*(4), 453–457.

Bosboom, R. E., Dupont-Nivet, G., Grothe, A., Brinkhuis, H., Villa, G., Mandic, O., … Krijgsman, W. (2014). Linking Tarim Basin sea retreat (West China) and Asian aridification in the late Eocene. *Basin Research*, *26*, 1–20.

Brandes, C., & Tanner, D. (2014). Fault-related folding: A review of kinematic models and thier application. *Earth-Science Reviews*, *138*, 352–370.

Burtman, V. S., & Molnar, P. (1993). Geological and geophysical evidence for deep subduction of continental crust beneath the Pamir. *Geological Society of America Special Papers*, *281*, 1–76. https://doi.org/10.1130/SPE281-p1

Casas, A. M., Gil, I., Leránoz, B., Millán, H., & Simón, J. L. (1994). Quaternary reactivation of flexural-slip folds by diapiric activity: Example from the western Ebro Basin (Spain). *Geologische Rundschau*, *83*, 853–867.

Chen, J., Scharer, K. M., Burbank, D. W., Heermance, R., & Wang, C. S. (2005). Quaternary detachment folding of theMingyaole anticline, southern Tian Shan [in Chinese]. *Seismology and Geology*, *27*, 530–547.

Chen, Y. G., Lai, K., Lee, Y., Suppe, J., Chen, W., Liu, Y., … Kuo, Y. (2007). Coseismic fold scarps and their kinematic behavior in the 1999 Chi-Chi earthquake Taiwan. *Journal of Geophysical Research*, *112*, B03S02. https://doi.org/10.1029/2006JB004388

Daëron, M., Avouac, J. P., & Charreau, J. (2007). Modeling the shortening history of a fault tip fold using structural and geomorphic records of deformation. *Journal of Geophysical Research*, *112*, B03S13. https://doi.org/10.1029/2006JB004460

Davis, G. H., Reynolds, S. J., & Kluth, C. F. (2012). *Structural geology of rocks and regions* (3rd ed.). (pp. 839). Hoboken: John Wiley & Son. Inc.

Feng, X. Y. (1994). Surface rupture associated with the 1985 Wuqia earthquake. In *Xinjiang [in Chinese], Research on Active Fault (3)* (pp. 45–55). Beijing: Seismological Press.

Gutiérrez, F., Carbonel, D., Mirkeham, R. M., Guerrero, J., Lucha, P., & Matthews, V. (2014). Can flexural-slip faults related to evaporate dissolution generate hazardous earthquakes? The case of the Grand Hogback monocline of west-central Colorado. *Geological Society of America Bulletin*, *126*(11-12), 1481–1494. https://doi.org/10.1130/B31054.1

Gutiérrez-Alonson, G., & Gross, M. R. (1999). Structures and mechanisms associated with development of a fold in the Cantabrian Zone thrust belt, NW Spain. *Journal of Structural Geology*, *21*(6), 653–670.

Heermance, R. V., Chen, J., Burbank, D. W., & Miao, J. J. (2008). Temporal constraints and pulsed Late Cenozoic deformation during the structural disruption of the active Kashi foreland, northwest China. *Tectonics*, *27*, TC6012. https://doi.org/10.1029/2007TC002226

Horne, R., & Culshaw, N. (2001). Flexural-slip folding in the Meguma Group, Nova Scotia, Canada. *Journal of Structural Geology*, *23*(10), 1631–1652.

Huang, W., Yang, X., Li, A., Pierce, I., Thompson, J. A., Angster, S. J., & Zhang, L. (2015). Late Pleistocene shortening rate on the northern margin of the Yanqi Basin, southeastern Tian Shan, NW China. *Journal of Asian Earth Sciences*, *112*, 11–24.

Huang, W., Yang, X., Li, A., Thompson, J. A., & Zhang, L. (2014). Climatically controlled formation of river terraces in a tectonically active region along the southern piedmont of the Tian Shan, NW China. *Geomorphology*, *220*, 15–29. https://doi.org/10.1016/j.geomorph.2014.05.024

Hubert-Ferrari, A., Suppe, J., Gonzalez-Mieres, R., & Wang, X. (2007). Mechanisms of active folding of the landscape (southern Tian Shan, China). *Journal of Geophysical Research*, *112*, B03S09. https://doi.org/10.1029/2006JB004362

Ishiyama, T., Mueller, K., Togo, M., Okada, A., & Takemura, K. (2004). Geomorphology, kinematic history, and earthquake behavior of the active Kuwana wedge thrust anticline, central Japan. *Journal of Geophysical Research*, *109*, B12408. https://doi.org/10.1029/2003JB002547

Jia, C., Zhang, S., & Wu, S. (2004). *Stratigraphy of the Tarim Basin and Adjacent Areas (in Chinese with English abstract)* (pp. 1063). Beijing: Science Press.

Kelsey, H. M., Sherrod, B. L., Nelson, A. R., & Brocher, T. M. (2008). Earthquakes generated from bedding plane-parallel reverse faults above an active wedge thrust, Seattle fault zone. *Geological Society of America Bulletin*, *120*(11-12), 1581–1597.

Krugh, W. C., & Meigs, A. (2003). Secondary deformation associated with active basement-involved folding; late Quaternary flexural-slip faulting and kink-band migration, Sierra de Villicum, San Juan, Argentina. *Geological Society of America*, *35*, 97. Abstracts with Programs

Lavé, J., & Avouac, J. P. (2000). Active folding of fluvial terraces across the Siwaliks Hills, Himalayas of central Nepal. *Journal of Geophysical Research*, *105*(B3), 5735–5770. https://doi.org/10.1029/1999JB900292

Lavé, J., & Avouac, J. P. (2001). Fluvial incision and tectonic uplift across the Himalaya of central Nepal. *Journal of Geophysical Research*, *106*(B11), 26561–26591.

Le Béon, M., Suppe, J., Jaiswal, M. K., Chen, Y. G., & Ustaszewski, M. E. (2014). Deciphering cumulative fault slip vectors from fold scarps: Relationships between long-term and coseismic deformations in central Western Taiwan. *Journal of Geophysical Research: Solid Earth*, *119*(7), 5943–5978. https://doi.org/10.1002/2013JB010794

Li, T., Chen, J., Fang, L., Chen, Z., Thompson, J. A., & Jia, C. (2016). The 2015 $M_w$ 6.4 Pishan earthquake: Seismic hazards of active blind wedge thrust system at the Western Kunlun range front, northwest Tibetan Plateau. *Seismological Research Letters*, *87*(3), 601–608. https://doi.org/10.1785/0220150205

Li, T., Chen, J., Thompson, J. A., Burbank, D. W., & Xiao, W. P. (2012). Equivalency of geologic and geodetic rates in contractional orogens: New insights from the Pamir Frontal Thrust. *Geophysical Research Letters*, *39*, L15305. https://doi.org/10.1029/2012GL051782

Li, T., Chen, J., Thompson, J. A., Burbank, D. W., & Yang, X. (2013). Quantification of three-dimensional folding using fluvial terraces: A case study from the Mushi anticline, northern margin of the Chinese Pamir. *Journal of Geophysical Research*, *112*, B03S09. https://doi.org/10.1029/2006JB004362

Li, T., Chen, J., Thompson, J. A., Burbank, D. W., & Yang, H. (2015a). Hinge-migrated fold-scarp model based on an analysis of bed geometry: A study from the Mingyaole anticline, southern foreland of Chinese Tian Shan. *Journal of Geophysical Research: Solid Earth*, *120*(9), 6592–6613. https://doi.org/10.1002/2015JB012102

Li, T., Chen, J., Thompson, J. A., Burbank, D. W., & Yang, X. (2015b). Active flexural-slip faulting: A study from the Pamir-Tian Shan convergent zone, NW China. *Journal of Geophysical Research: Solid Earth*, *120*(6), 4359–4378. https://doi.org/10.1002/2014JB011632

Li, T., Chen, J., & Xiao, W. (2013). Late-Quaternary folding of the Mingyaole anticline southwestern tip, Pamir-Tianshan convergent zone [in Chinese]. *Seismology and Geology*, *35*, 234–246.

Lisiecki, L. E., & Raymo, M. E. (2005). A Pliocene-Pleistocene stack of 57 globally distributed benthic $\delta^{18}$O records: PLIOCENE-PLEISTOCENE BENTHIC STACK. *Paleoceanography*, *20*, PA1003. https://doi.org/10.1029/2004PA001071

Lu, H., Burbank, D. W., & Li, Y. (2010). Alluvial sequence in the north piedmont of the Chinese Tian Shan over the past 550 kyr and its relationship to climate change. *Palaeogeography Palaeoclimatology Palaeoecology*, *285*(3-4), 343–353.

Malatesta, L., Prancevic, J., & Avouac, J. P. (2016). Autogenic entrenchment patterns and terraces due to coupling with lateral erosion in incising alluvial channels. *Journal of Geophysical Research: Earth Surface*, *122*(1), 335–355. https://doi.org/10.1002/2015JF003797

McInelly, G. W., & Kelsey, H. M. (1990). Late Quaternary tectonic deformation in the Cape Arago-Bandon region of coastal Oregon as deduced from wave-cut platforms. *Journal of Geophysical Research*, *95*(B5), 6699–6713.

Mitra, S. (2002). Structural models of faulted detachment folds. *AAPG Bulletin*, *86*, 1673–1694.

Molnar, P., Brown, Burchfiel, B. C., Deng, Q., Feng, X., Li, J., … You, H. (1994). Quaternary climate change and the formation of river terraces across growing anticlines on the north flank of the Tien Shan, China. *Journal of Geology*, *102*(5), 583–602.

Niño, F., Philip, H., & Chery, J. (1998). The role of bed-parallel slip in the formation of blind thrust faults. *Journal of Structural Geology*, *20*(5), 503–516.

Pan, B., Burbank, D. W., Wang, Y., Wu, G., Li, J., & Guan, Q. (2003). A 900 k.y. record of strath terrace formation during glacial-interglacial transitions in northwest China. *Geology*, *31*(11), 957–960.

Philip, H., & Meghraoui, M. (1983). Structural analysis and interpretation of the surface deformations of the El Asnam earthquake of October 10, 1980. *Tectonics*, *2*(1), 17–49.

Poblet, J. (2012). 2D kinematic models of growth fault-related folds in contractional settings. In C. Busby, & A. Azor (Eds.), *Tectonics of sedimentary basin: Recent advances* (1st ed.) (pp. 538–564). West Sussex, UK: Wiley-Blackwell.

Poblet, J., & McClay, K. (1996). Geometry and kinematics of single-layer detachment folds. *American Association of Petroleum Geologists Bulletin*, *80*, 1085–1109.

Poblet, J., McClay, K., Storti, F., & Muñoz, J. (1997). Geometries of syntectonic sediments associated with single-layer detachment folds. *Journal of Structural Geology*, *19*(3-4), 369–381.

Poisson, B., & Avouac, J. P. (2004). Holocene hydrological changes inferred from alluvial stream entrenchment in North Tian Shan (northwestern China). *Journal of Geology*, *112*(2), 231–249.

Ramsay, J. G. (1967). *Folding and fracturing of rocks*. New York: McGrawHill.

Ramsay, J. G. (1974). Development of chevron folds. *Bulletin Geological Society of America*, *85*(11), 1741–1754.

Rockwell, T. K., Keller, E. A., & Clark, M. N. (1984). Chronology and rates of faulting of Ventura River terraces, California. *Geological Society of America Bulletin*, *95*(12), 1466–1474.

Rockwell, T. K., Keller, E. A., & Dembrof, G. R. (1988). Quaternary rate of folding of the Ventura Avenue anticline, western Transverse Ranges, southern California. *Geological Society of America Bulletin*, *100*(6), 850–858.

Roering, J. J., Cooke, M. L., & Pollard, D. D. (1997). Why blind thrust faults do not propagate to the Earth's surface: Numerical modeling of coseismic deformation associated with thrust-related anticlines. *Journal of Geophysical Research*, *102*(B6), 11,901–11,912.

Saint-Carlier, D., Charreau, J., Lavé, J., Blard, P., Dominguez, S., Avouac, J., … Team, A. (2016). Major temporal variations in shortening rate absorbed along a large active fold of the southeastern Tianshan piedmont (China). *Earth and Planetary Science Letters*, *434*, 333–348.

Sanz, P. F., Pollard, D. D., Allwardt, P. F., & Borja, R. I. (2008). Mechanical models of fracture reactivation and slip on bedding surfaces during folding of the asymmetric anticline at Sheep Mountain, Wyoming. *Journal of Structural Geology*, *30*(9), 1177–1191.

Scharer, K. M., Burbank, D. W., Chen, J., & Weldon, R. J. II (2006). Kinematic models of fluvial terraces over active detachment fold: Constraints on the growth mechanism of the Kashi-Atushi fold system, Chinese Tian Shan. *Geological Society of America Bulletin*, *118*(7-8), 1006–1021. https://doi.org/10.1130/B25835.1

Shaw, J. H., Connors, C., & Suppe, J. (2005). *Seismic Interpretation of Contractional Fault-Related Folds* (Vol. 53) AAPG Studies in Geology Tulsa, OK: American Association of Petroleum Geologists.

Simoes, M., Avouac, J. P., Chen, Y., Singhvi, A. K., Wang, C., Jaiswal, M., … Bernard, S. (2007). Kinematic analysis of the Pakuashan fault tip fold, west central Taiwan: Shortening rate and age of folding inception. *Journal of Geophysical Research*, *112*, B03S14. https://doi.org/10.1029/2005JB004198

Sobel, E. R., Chen, J., & Heermance, R. V. (2006). Late Oligocene-Early Miocene initiation of shortening in the southwestern Chinese Tian Shan: Implications for Neogene shortening rate variations. *Earth and Planetary Science Letters*, *247*(1-2), 70–81. https://doi.org/10.1016/j.epsl.2006.03.048

Sobel, E. R., Chen, J., Schoenbohm, L. M., Thiede, R., Stockli, D. F., Sudo, M., & Strecker, M. (2013). Oceanic-style subduction controls late Cenozoic deformation of the Northern Pamir orogen. *Earth and Planetary Science Letters*, *363*, 204–218.

Sun, J., Xiao, W., Windley, B. F., Ji, W., Fu, B., Wang, J., & Jin, C. (2016). Provenance change of sediment input in the northeastern foreland of Pamir related to collision of the Indian Plate with the Kohistan-Ladakh arc at around 47 Ma. *Tectonics*, *35*(2), 315–338. https://doi.org/10.1002/2015TC003974

Suppe, J., Sabat, F., Munoz, J. A., Poblet, J., Roca, E., & Verges, J. (1997). Bed-by-bed fold growth by kink-band migration: Sant Llorenc de Morunys, eastern Pyrenees. *Journal of Structural Geology*, *19*(3-4), 443–461. https://doi.org/10.1016/S0191-8141(96)00103-4

Tanner, P. (1989). The flexural-slip mechanism. *Journal of Structural Geology*, *11*(6), 635–655.

Tavani, S., Storti, F., Lacombe, O., Corradetti, A., Muñoz, J. A., & Mazzoli, S. (2015). A review of deformation pattern templates in foreland basin systems and fold-and-thrust belts: Implications for the state of stress in the frontal regions of thrust wedges. *Earth-Science Reviews*, *2015*(141), 82–104.

Thompson, J. A. (2013). Neogene tectonic evolution of the NE Pamir margin, NW China, PhD thesis, University of California, Santa Barbara.

Thompson, J. A., Burbank, D. W., Li, T., Chen, J., & Bookhagen, B. (2015). Late Miocene northward propagation of the northeast Pamir thrust system, northwest China. *Tectonics*, *34*(3), 510–534. https://doi.org/10.1002/2014TC003690

Thompson, S. C., Weldon, R. J., Rubin, C. M., Abdrakhmatov, K., Molnar, P., & Berger, G. W. (2002). Late Quaternary slip rates across the central Tien Shan, Kyrgyzstan, central Asia. *Journal of Geophysical Research*, *107*(B9), ETG 7-1–ETG 7-32, 2203. https://doi.org/10.1029/2001JB000596

Walker, R., Jackson, J., & Baker, C. (2003). Surface expression of thrust faulting in eastern Iran: Source parameter and surface deformation of the 1978 Tabas and 1968 Ferdows earthquake sequences. *Geophysical Journal International*, *152*(3), 749–765.

Wang, X., Suppe, J., Guan, S. W., Hubert-ferrari, A., & Jia, C. (2011). Cenozoic structure and tectonic evolution of the Kuqa foldbelt, southern Tianshan, China. In K. R. McClay, J. Shaw, & J. Suppe (Eds.), *Thrust Fault-Related Folding* (*AAPG Mem*) (pp. 215–243).

Wang, Z., & Wang, X. (2016). Late Cenozoic deformation sequence of a thrust system along the eastern margin of Pamir, northwest China. *Acta Geologica Sinica*, *90*(5), 1664–1678.

Wei, H. H., Meng, Q., Ding, L., & Li, Z. (2013). Tertiary evolution of the western Tarim basin, northwest China: A tectono-sedimentary response to northward indentation of the Pamir salient. *Tectonics*, *32*(3), 558–575. https://doi.org/10.1002/tect.20046

Yang, S. M., Li, J., & Wang, Q. (2008). The deformation pattern and fault rate in the Tianshan Mountains inferred from GPS observations. *Science in China Series D*, *51*(8), 1064–1080. https://doi.org/10.1007/s11430-008-0090-8

Yeats, R. S., Clark, M. N., Keller, E. A., & Rockwell, T. K. (1981). Active fault hazard in south California Ground rupture versus seismic shaking. *Geological Society of America Bulletin*, *92*(4), 189–196.

Yeats, R. S., Sieh, K. S., & Allen, C. R. (1997). *Geology of Earthquake*( pp. 344–346). New York: Oxford University Press.

Yin, A., Nie, S., Craig, P., Harrison, T. M., Ryerson, F. J., Qian, X., & Yang, G. (1998). Late Cenozoic tectonic evolution of the southern Chinese Tian Shan. *Tectonics*, *17*(1), 1–27. https://doi.org/10.1029/97TC03140

Zubovich, A. V., Wang, X.-Q., Scherba, Y. G., Schelochkov, G. G., Reilinger, R., Reigber, C., … Beisenbaev, R. T. (2010). GPS velocity field of the Tien Shan and surrounding regions. *Tectonics*, *29*, TC6014. https://doi.org/10.1029/2010TC002772